Durham E-Theses

Impact of Graphene Quantum Dot Edge Shapes on High-Performance Energy Storage Devices

GILLEECE, GRAINNE

How to cite:

Use policy

Impact of Graphene Quantum Dot Edge Shapes on High-Performance Energy Storage Devices

Grainne Gilleece

Supervised by Dagou Zeze and Natasha Shirshova

Department of Engineering

Durham University

A thesis presented for the degree of

Master of Science by Research

2023

Abstract

Graphene quantum dots (GQDs) are a promising electrode material for the advancement of energy storage devices due to their fast-moving charge carriers, high surface area to volume ratio and controllable bandgaps. However, the differences between the electronic properties of zigzag and armchair-edged graphene quantum dots (GQDs) have not yet been well defined and are explored in detail in this work.

Nitrogen-doped GQDs with zigzag (ZZ) and armchair (AC) edges were synthesised hydrothermally and electrochemically, respectively. Surface (XRD, TEM, UV-Vis) characterisation was conducted on the synthesised GQDs. It was found that the bandgap of ZZ GQDs is controllable through pH variation and size variations dictated by synthetic reaction times, while this is not the case for AC GQDs. ZZ and AC GQDs were electrodeposited on the surface of carbon fibre electrodes. Electrochemical characterisation (cyclic voltammetry, electrical impedance spectroscopy) was carried out on these electrodes. The specific capacitance of all carbon fibre electrodes increased upon the deposition of GQDs, with the greatest increase observed to be a 275 % improvement in specific capacitance upon the addition of 5 nm zigzag GQDs. Carbon fibre electrodes with deposited ZZ GQDs display a more significant increase in capacitance values (specific capacitance, electrical double layer capacitance, pseudocapacitance and quantum capacitance) due to a greater affinity for edge site doping and a larger surface area compared to AC GQD carbon fibre electrodes. ZZ GQDs are therefore more beneficial for energy storage devices than AC GQDs.

Table of Contents

1. Introduction

The fabrication of sustainable high-performance energy storage devices is more important than ever amid the Global Energy Crisis. Environmental pollution and the rapid depletion of fossil fuels have turned attention to renewable energy sources, including solar, wind and geothermal. These energy sources provide energy intermittently, meaning the generated energy needs to be stored for later release. Furthermore, the increased popularity of electric vehicles demands improvement in energy storage technologies. Electrochemical energy storage devices such as batteries and supercapacitors are thus being heavily researched to develop new, high-performance devices to meet these energy storage needs.

The development of high-performance energy storage devices requires a careful selection of electrode materials. Conductivity, stability, surface area etc. are all essential considerations for the performance optimisation of energy storage devices. One with great potential to improve the performance of these devices is zero-dimensional graphene quantum dots (GQDs), which can be used to modify electrodes. GQDs are nanometre-sized semiconductor particles consisting of only one or a few layers of graphene[1]. GQDs were first synthesised by Ponomarenko and Geim in 2008[2]. They possess discrete energy levels which can be precisely controlled by altering the nanoparticles' size, shape and edges, resulting in tuneable electronic and photoluminescence properties.

GQDs display the same highly crystalline structure as graphene sheets. They are allotropes of carbon that exist as hexagonal lattice structures. Each carbon atom is covalently bonded to three others and establishes a trigonal planar geometry, resulting in sp^2 hybridisation. The fourth electron (in the p orbital) is unbonded, leading to the delocalisation of the π electrons perpendicular to the plane of the particle [3] and consequently high conductivity due to the high mobility of these delocalised electrons. GQDs typically contain a few layers of graphene held together by Van der Waals forces.

Despite the recent increase in research on GQDs[4]–[6], the practical implications of altering the shape and structure of the nanoparticles on the devices into which they are integrated have not been investigated in detail. Additionally, little is known about the chemical kinetics of GQDs on electrode surfaces. This information is essential for optimising the performance of the devices and is investigated in this work.

To understand why GQDs are an optimal material for furthering the development of energy storage devices, it is worth mentioning some of their important properties. GQDs maintain several of graphene's unique properties, such as high charge carrier mobility, thermal conductivity, and

physical and chemical resistance[7]. GQDs, however, also display additional electronic and photoluminescence properties due to the quantum confinement effect.

1.1. Quantum Confinement Effect in GQDs

2D graphene is a zero-bandgap semimetal as a result of the six Dirac points in the material[8]. The emergence of a bandgap can be achieved through the quantum confinement effect in graphene quantum dots, whereby discrete energy levels form when the particle's size reaches the nanoscale. Quantum confinement effects become evident when the particle's lateral radius is comparable to or smaller than the Bohr radius of an exciton, and the excitons are therefore confined in all three dimensions. For this reason, GQDs are known as a zero-dimensional material[9].

The exact size at which bulk graphene begins to display confinement properties is not well defined. The bulk exciton Bohr radius (a_B) is typically calculated using:

$$a_B = a_0 \varepsilon \frac{m_0}{\mu} \qquad (1)$$

where a_0 is the Bohr radius of a hydrogen atom, ε is the dielectric permittivity of the bulk material, m_0 is the mass of a free electron and μ is the exciton reduced mass[10]. Issues arise when applying this model to bulk graphene. The charge carriers in bulk graphene behave as massless Dirac fermions due to the linear intersection of its conduction and valence bands[11]. The zero effective mass of these particles thus results in graphene displaying an infinite Bohr radius and so graphene can theoretically display confinement properties at any finite size[9]. Despite this, it has previously been observed that quantum confinement effects only become prevalent when the particle reaches around 100 nm[2]. GQDs are thus defined to be graphene particles with a lateral dimension of less than 100 nm. As a note, a small energy gap can be seen in bilayer graphene, however these are not considered to be quantum dots since the bandgap is induced by an applied bias rather than through 3D spatial constraints, and the material is 2 dimensional[12]. Similarly, a bandgap is observed in graphene nanoribbons, however the charge carriers in these are only confined in 2 dimensions, and are again separate from quantum dots[13].

Quantum confinement in GQDs is size, shape, and edge dependent[14]; altering these causes the particle's bandgap to widen or narrow and therefore affects its electronic properties.

GQDs can possess zigzag (ZZ) edges, armchair (AC) edges, or a combination of these (*Figure 1*). ZZ edges are carbene-like, where each carbon atom at the edges of the particle contains two unshared valence electrons. AC edges have triple bonds between the carbon atoms at the edges of the GQD, a carbyne-like structure[3]. This therefore results in sp hybridisation at the edges of armchair GQDs.
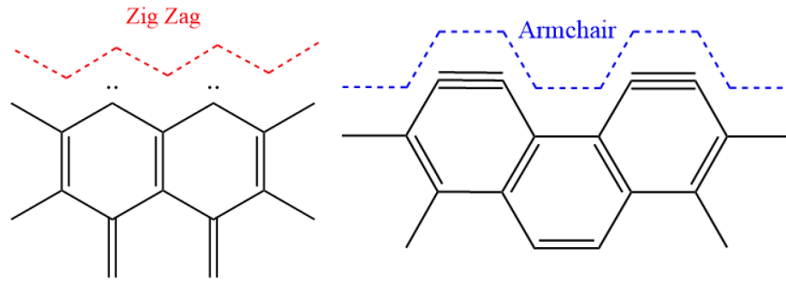
Figure 1:   *Zigzag and armchair GQD edges*

The ground state of a conventional quantum dot is localised in the centre of the particle, while the ground state of the conduction and valence band localise in the centre of each edge for hexagonal ZZ GQDs[15]. This results from the charge carriers behaving as confined photons in a cavity, where the eigenmodes of the photons that propagate azimuthally around and are confined to the cavity (whispering gallery modes) localise at its boundary. As a direct result of this phenomenon, the bandgap of hexagonal ZZ quantum dots decays to zero rapidly as the size of the GQD increases. This is only the case for hexagonal ZZ GQDs since each carbon atom contributes differently to the edge state of the GQD. This does not occur in hexagonal AC GQDs, meaning the density distribution of the ground state conduction and valence bands for these structures is more evenly distributed over the whole particle.

In most GQDs, the bandgap changes according to the relation:

$$E_{gap} \propto \frac{1}{\sqrt{N}} \tag{2}$$

where *N* is the number of atoms in the GQD (both carbon and hydrogen)[16]. This is also the case for square GQDs with a combination of ZZ and AC edges[17]. The bandgap of GQDs is typically between ~1.9 and 3.4 eV[18], [19]. The bandgap will not reach zero for any dimension of GQDs since, as mentioned above, quantum confinement doesn't become dominant until the particle is under 100 nm. In addition to this, the bandgap will not become extremely wide as the minimum size of GQDs is ~2 nm[20].

Synthesising GQDs is unlikely to result in uniform hexagonal-shaped GQDs; however, it should be noted that AC-edged GQDs have a wider bandgap than ZZ GQDs of the same size[21]. Since the energy gap relation in equation (2) is true for most GQD shapes, knowledge of the overall shape of the GQDs is of low concern but should be acknowledged.

1.2. Density of states

The hexagonal structure of graphene can be thought of as two superimposed triangular sublattices (*Figure 2*), which are similar by inversion symmetry.
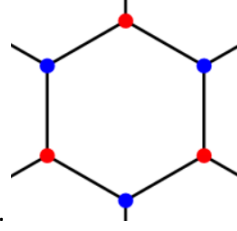
Figure 2: *Graphene lattice structure. The red and blue represent the different sublattices.*

AC and ZZ-edged GQDs will display a different density of states at their Fermi level. This is a result of the sublattice geometry at their edges. The atoms at the edges of ZZ GQDs are all the same sublattice type, whereas AC GQDs terminate with an atom from each sublattice, resulting in non-identical boundary conditions describing the Hamiltonians of each edge shape. For a ZZ GQD, the wavefunction will vanish for a single sublattice at its edge, resulting in its lowest Landau level supporting two types of edge states (current carrying and dispersionless)[22]. One of these edge states (dispersionless) does not pass through the Fermi level for any non-zero doping. For AC edges, the wavefunction will vanish for both sublattices and only current carrying edge states are observed. Consequently, ZZ GQDs will always display a larger density of states at their Fermi level[23]. Simulated DOS profiles for both armchair edged and zigzag edged GQDs are displayed in *Figure 3.*
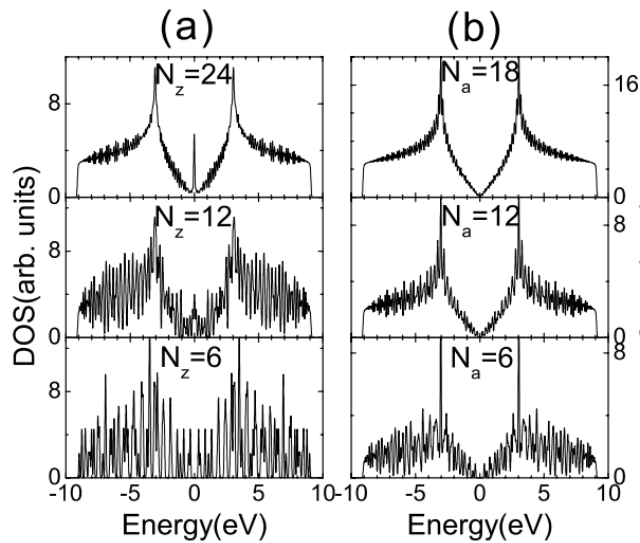
Figure 3: *Simulated DOS diagrams for a) zigzag edged GQDs and b) armchair edged GQDs. N represents the number of hexagonal rings in the quantum dot*[24]*.*

Despite the noted difference in the bandgap and density of states of GQDs with different edge shapes, *little work has been done to determine how these differences impact electronic devices upon GQD embedding*.

2. Energy Storage in Graphene Quantum Dots

2.1. Energy storage mechanisms of GQDs

The addition of GQDs to energy storage devices can increase their overall storage capability. GQDs store energy through two processes, namely electrical double layer capacitance and pseudocapacitance. The total capacitance, however, is limited by the quantum capacitance[25].

2.1.1. Electrical Double Layer Capacitance

An electrical double layer (EDL) is the interface between a charged surface (electrode) and an electrolyte across which an electric field exists[26]. It consists of an immobile layer of ions in the electrolyte, which remains fixed to the oppositely charged electrode. The layer is approximately one ion thick and is known as the Helmholtz layer. This layer is split into two sublayers: the inner Helmholtz plane (IHP) and the outer Helmholtz plane (OHP). The IHP passes through the centres of specifically adsorbed ions, whereby ions that have partially or fully lost their solvation shells are adsorbed close to the surface of the electrode. The OHP passes through the centre of the solvated ions closest to the surface of the electrode[27]. The remaining charges are mobile in a diffuse layer (or Gouy-Chapman layer), beyond the OHP[28]. It was demonstrated by Bockris *et al.* [29] that in the IHP, the solvent molecules orientate under the influence of an electric field in the direction of the field. In contrast, in the OHP, the solvent molecules orientate towards the solvated ion.

This model results in a linear decrease in electric potential across the Helmholtz layer and a quasi-exponential drop in potential from the beginning of the diffuse layer into the bulk solution. The overall differential capacitance is:

$$\frac{1}{C_d} = \frac{1}{C_H} + \frac{1}{C_{GC}} \tag{3}$$

where C_H is the Helmholtz capacitance, and C_{GC} is the Gouy-Chapman capacitance. At dilute electrolyte concentrations, the double layer is essentially all diffuse and so $C_d \approx C_{GC}$, while at high concentrations, the double layer is virtually all fixed and $C_d \approx C_H$.

For completeness, it should be noted that the Helmholtz capacitance is given by:

$$C_H = \frac{\varepsilon_r \varepsilon_0}{H} \tag{4}$$

where ε_r is the relative permittivity, ε_0 is the permittivity of a vacuum and H is the double layer distance, while the Gouy-Chapman capacitance is given by:

$$C_{GC} = \frac{2zeN_A c \lambda_D}{\psi_D} \sinh\left(\frac{ze\psi_D}{2k_B T}\right) \tag{5}$$

where e is the elementary charge, N_A is Avogadro's number, z is the charge of the electrolyte, c_∞ is the molar concentration of the electrolyte in the bulk solution, ψ_D is the electric potential in the diffuse layer, T is the temperature of the system, k_B is the Boltzmann constant, and λ_D is the Debye length[30].

When a potential is applied to the electrodes, the Helmholtz layer assembles at the surface of the electrode with opposite polarity to that of the electrolyte (*Figure 4*). The Helmholtz layer consists of an electrical space charge from the electrode side and an ion space charge from the electrolyte side[31], allowing electrical energy to accumulate in this layer and acting as a charge storage mechanism. EDLCs store energy electrostatically, meaning no chemical reactions occur (energy is stored in a static state).
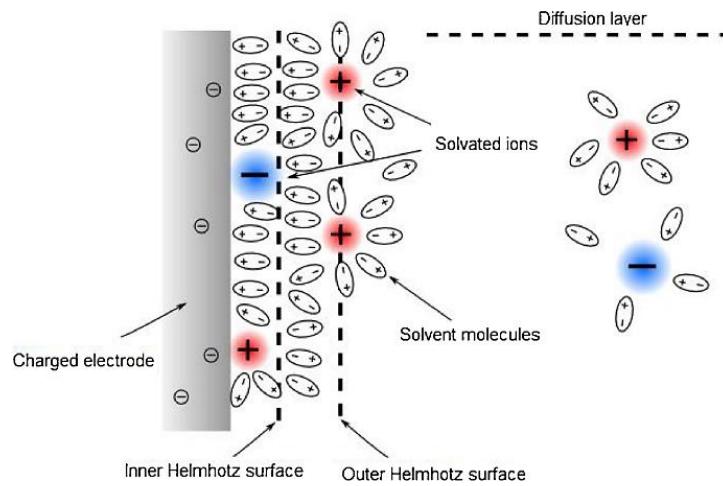
Figure 4: *Electrical double layer (EDL) structure*[32]

2.1.2. Pseudocapacitance

For an electrode possessing Faradaic materials on its surface, fast and reversible redox reactions occur at the electrode-electrolyte interface under applied potential. Energy is stored electrostatically through these redox reactions[33].

2.1.3. Quantum Capacitance

Nanostructured materials suffer from an intrinsic limiting factor to their total capacitance, known as quantum capacitance. Quantum capacitance (C_q) acts in series with traditional electrostatic capacitance according to the equation:

$$\frac{1}{C_{total}} = \frac{1}{C_{dl}} + \frac{1}{C_q} \qquad (6)$$

where C_{total} is the total capacitance, and C_{dl} is the double layer capacitance[25]. The phenomenon results from poor screening, leading to a depolarising field effect opposite to the dielectric

polarisation. This then leads to a reduction in field line cancellations due to the subdued polarisation[34], ultimately limiting the electrode's ability to accumulate charge on its surface in response to the electrode's potential[35].

Graphene-based materials undergo imperfect screening due to their low density of free electrons[36]. The quantum capacitance is directly related to the material's density of states by the equation:

$$C_q = e\sqrt{\varepsilon \varepsilon_0 D(E_F)} \tag{7}$$

where C_q is the quantum capacitance, e, ε and ε_0 are the elementary charge, the dielectric permittivity of the material, and the vacuum permittivity, respectively, and $D(E_F)$ is the density of states[25].

The limiting effects of quantum capacitance of GQDs can be improved by heteroatom doping, functionalisation and the introduction of defects to the lattice structure.

2.2. Defects in GQDs

GQDs can possess point or line defects to their lattice structure. Defects cause breakage of the electron-hole symmetry, leading to changes in the electronic structure of the nanoparticles while increasing their chemical reactivity. A defect-induced increase in the density of states of the GQDs increases the quantum capacitance of the material, reducing the limitations to the total capacitance it causes. Moreover, the defects in the structure can be zigzag or armchair like, whereby the removal of atoms in the centre of the graphene lattice leaves behind defect structures that terminate in either carbene or carbyne-like bonds (*Figure 5*). Due to the presence of dispersionless edge states, zigzag edge-type defects will increase the density of states of the nanoparticles to a greater extent than armchair edge type defects[37], further increasing the quantum capacitance.

Defects have further benefits for energy storage devices since they provide increased diffusion channels, more vacancies and edges for ion access, and a larger surface area upon which the double layer can form[38].
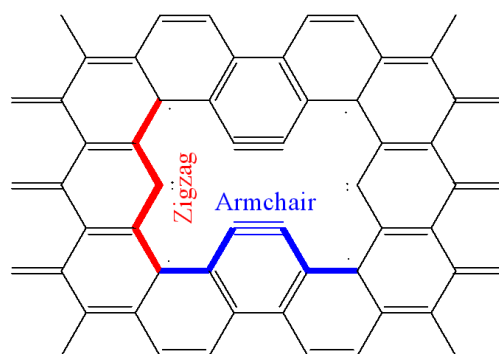
Figure 5:   *A GQD with defects in its lattice structure. Carbon atoms have been removed from the centre of the structure, leaving zigzag and armchair-type defects.*

2.3. Heteroatom Doped GQDs

Carbon atoms in the GQD lattice structure can be replaced by heteroatoms through heteroatom doping, altering the structure and electronic properties of the nanoparticles. The configuration of the doped atoms, particularly whether they are doped on their basal plane or edge sites, influences the electronic properties to different extents. The doping of heteroatoms introduces defect energy levels and causes a shift in the Fermi level position, thereby altering the bandgap of the GQDs. Depending on whether the doped atoms are electron withdrawing or donating, the bandgap may be widened or narrowed by heteroatom doping [39].

Electrical conductivity is typically improved upon increasing doping concentration[40]. However, this is only up to a point since the insertion of an extremely large number of heteroatoms will compromise the inherent graphene structure.

The heteroatom sites are defects in the crystal structure. They can provide more ion diffusion channels for adsorption, alongside a higher number of active sites, improving wettability and decreasing charge transfer resistance. Heteroatom doping also leads to a higher charge carrier density, increasing the volumetric capacity of the GQDs. Furthermore, higher carrier density improves conductivity through faster electron transport in the nanoparticles, increasing the quantum capacitance and introducing pseudocapacitance through the redox-active heteroatoms, therefore increasing the doped GQDs' specific capacitance[41].

GQDs are most commonly doped with nitrogen, boron, sulfur, or phosphorous. These heteroatoms have all been shown to increase the capacitance of GQDs due to the reasons outlined above, but each has its drawback. The extent of nitrogen doping is difficult to control, and the configuration of

the doped nitrogen has a significant impact on the capacitance of the nanoparticles[40] and will be explored in section 4.1. P doping can broaden the electrochemical window of the electrode; however, phosphorous doping of GQDs typically reduces their conductivity due to the large atomic size of P compared to C, alongside its vacant 3d orbital. Similarly, doping GQDs with sulfur can decrease the conductivity of the nanoparticles. This results from the different bond lengths of C-S compared to C-C, which can cause a curvature in the graphene plane[42]. Boron doping is promising for improving the electrochemical performance of the nanoparticles[43]; however the doping process is considerably more complex than doping with other heteroatoms, and B-doped GQDs are therefore less investigated.

2.4. Functionalised GQDs

Further to edges, shape and particle size, chemical functionalisation of GQDs affects quantum confinement. Functionalisation occurs through covalent bonding through reactions with residual groups present on the GQDs or, more commonly, noncovalent bonding via hydrogen bonding, van der Wals force, π-π stacking, electrostatic interaction or chemisorption[44], [45]. Functionalisation differs from heteroatom doping since functionalised groups are not a part of the lattice structure of the GQDs. The functionalisation of GQDs can narrow their bandgap due to the increase in relative nanoparticle size.

To add to the electronic benefits of functionalisation, the functionalisation of GQDs also provides several chemical benefits when integrated into energy storage devices. Functionalisation can occur between graphite layers in GQDs and improve solvent dispersibility, shorten ion diffusion distances and increase the number of active sites present. The functional groups increase the wettability of the electrode, leading to enhanced electrolyte adsorption and promoting the formation of the electrical double layer[46]. Furthermore, the functional groups are Faradaic and lead to a pseudocapacitive contribution to the total capacitance of the GQDs.

Oxygen-rich functional groups are introduced to GQDs synthesised from oxygen-containing precursors and are present on almost all GQDs. Carbonyl and quinone groups primarily contribute a pseudocapacitive effect in acidic electrolytes, while carboxyl groups provide Faradaic reactions in basic electrolytes[47].

The introduction of functional group to edge sites of GQDs causes steric effects. When the edge sites of zigzag GQDs are passivated only by hydrogen atoms, steric effects caused by hydrogen are negligible since the carbon carbon distance (2.46 Å) is more than double the van der Waals radius of hydrogen (1.10 Å)[48]. When these hydrogen atoms are replaced by functional groups, steric hindrance begins to take place and rippling occurs at the edges of the particle, becoming more

prevalent as the size of the functional group increases. The proximity of functional groups to other functional groups on the edges of the particle will evidently make a large difference to the extent of geometric changes of the GQD; the closer the functional groups are to each other, the greater the steric hindrance. The changes in planarity of the GQD affect its bandgap, decreasing its size by up to ~0.3 eV[49]. The largest changes in energy gap will occur for functionalised GQDs where the functional groups are located on the GQD in such a way that molecular symmetry is preserved (e.g. a triangular GQD with a functional group on each corner) as these particles will retain zero energy state degeneracy of planar GQDs, while still increasing exciton localisation within the structure[50]. The steric effects of functionalisation of GQDs have only been studied through DFT simulations thus far, and have not been investigated for synthesised GQDs with random shapes and uncontrollable locations of functional groups. For this reason, the changes in planarity of the nanoparticles due to functionalisation are beyond the scope of this thesis and are therefore not mentioned further. As a note, while it has not been explicitly investigated, armchair edge terminated pristine GQDs likely exhibit some form of steric effect due to the sp carbon triple bond at their edges, which is shorter than the sp^2 bonds at the edges of pristine zigzag GQDs and therefore likely distorts the outermost rings to some extent. This is, again, beyond the scope of this thesis.

2.5. GQDs as an Electrode Material

GQDs are an ideal material for integration into the electrodes of electrochemical energy storage devices since they have high conductivity, a large active surface area to volume ratio, rich active sites, and high thermal and chemical stability[51]. Their two energy storage mechanisms enhance the capacitance of the devices and boost rate capability. The addition of GQDs to electrodes improves their performance by increasing conductivity, number of active sites, and ion diffusion. They regulate electrode structure during the charge/ discharge process, improve kinetics, and increase electrode surface area.

GQDs cannot be used alone as an electrode material due to their tendency to agglomerate due to their strong π-π interactions. The aggregation results in a decreased surface area, thereby reducing the electrochemically active sites of the material. Furthermore, nanoparticle size will increase, decreasing the bandgap width. Upon excessive agglomeration, the GQDs will restack into graphene or graphite.

Instead, GQDs are deposited onto or embedded into other materials to form nanocomposite electrodes. Deposition methods include stirring attachment, chemical vapour deposition and electrophoretic deposition[46], while embedding is usually carried out through hydrothermal processes [52].

2.5.1. GQDs as a Supercapacitor Electrode Material

Supercapacitors are electrochemical energy storage devices which store charge through electrical double layer capacitance, pseudocapacitance, or both. They consist of an anode, a cathode, an electrolyte, and a separator between the electrodes, which prevents the occurrence of a short circuit. Since no chemical reactions take place, the energy is stored electrostatically. Further to redox pseudocapacitance outlined above, there are two other pseudocapacitive storage mechanisms through which supercapacitors can store charge (*Figure 6*). The first type is underpotential deposition (adsorption pseudocapacitance) [53]. This involves the adsorption of a monolayer on the surface of the electrode due to the reduction of a different metal ion, leading to a lowering of the potential in comparison to the equilibrium potentials of the metals [54]. The final type of pseudocapacitance is intercalation pseudocapacitance, displayed by some layered materials. Electrolyte ions are intercalated between layers of the material, causing the material to undergo Faradaic charge transfer, allowing fast and reversible charge storage [55]. Pseudocapacitors generally possess a higher capacitance than electrical double layer capacitors (EDLCs); however, the electrodes of pseudocapacitors increase in size during the charging process and decrease in size upon discharging, resulting in a shorter cycle life than EDLCs [56].
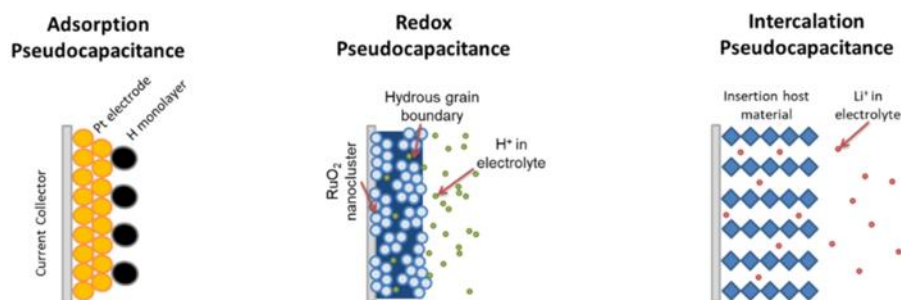
Figure 6*:   Different types of pseudocapacitance* [53]

Supercapacitors have gained attention in recent years for their potential as high-performance energy storage devices due to their long cycle lives (since electrode degradation is limited as no chemical reactions occur on their surfaces), short charging times, and high power densities. However, applications have been found to be somewhat limited due to their low energy density [57]. The energy density of supercapacitors can be boosted by increasing either the voltage window or their specific capacitance[58]. The specific capacitance of the devices can be increased by modifying the supercapacitor electrode materials. One way to achieve this is to deposit or embed GQDs onto/ into the electrodes. GQDs have therefore been investigated as an electrode material for supercapacitors to improve limitations to their energy density[52], [59]–[65].

Metal oxides and hydroxides are commonly used as pseudocapacitor electrodes. $Ni(OH)_2$ is a Faradaic material with a high theoretical capacitance, high stability in alkaline electrolytes, and is very abundant. However, $Ni(OH)_2$ has poor electrical conductivity in practice in contrast to its theoretical value as a result of discrepancies in its crystal structure, resulting in low rate capability and poor cycle stability due to structural changes during the charging/ discharging process. To counter this, Hong *et al*. [62] created binder-free electrodes using hydrothermal methods to embed GQDs in $Ni(OH)_2$ grown on a carbon cloth current collector. The GQDs were synthesised via a hydrothermal method using an autoclave from citric acid. The highly conductive GQDs stabilised the structure of the electrodes while also allowing fast transport of charge carriers. The GQDs also promoted ion diffusion of the electrolyte into the nanostructure of the electrode and prevented damage during the cycle process. The specific capacitance of the GQD-$Ni(OH)_2$ electrode was measured using a galvanostatic charge-discharge curve at 1 A/g in 2 M KOH electrolyte and was found to be 1825 F/g. $Ni(OH)_2$ on carbon cloth (i.e. the same electrode without embedded GQDs) has a specific capacitance of 545 F/g at 1 A/g in 2 M KOH electrolyte.

Carbon-based materials are often used as EDLC electrodes. Activated carbons are low-cost materials with a high surface area but are limited in performance by their porous structure. The structure disrupts the conductive networks, leading to a reduction in conductivity. Moreover, the micropore structure hinders electrolyte ion transport and storage. Qing *et al*. [63] took advantage of the nanometre size of GQDs to intersperse the activated carbon structure to construct overall conductive networks. The GQDs were synthesised by chemical oxidation using coal powder as a precursor. The GQDs enhanced the electrode structure and improved conductivity while additionally increasing the surface area of the electrodes, thus increasing the surface area on which the electrical double layer can form. Activated carbon was measured to have a specific capacitance of 246 F/g at 1 A/g in 6 M KOH electrolyte. In comparison, the GQD-activated carbon electrodes displayed a specific capacitance of 388 F/g at 1 A/g in 6 M KOH electrolyte.

In all reports [52], [59]–[65], the addition of GQDs benefits supercapacitor electrodes, improving their specific capacitance and therefore their energy density.

2.5.2. GQDs as a Battery Electrode Material

Lithium-ion batteries (LiBs) are currently the leading energy storage technology for portable electronic devices, electric vehicles, and global grid battery storage. Modern lithium-ion batteries encompass many different chemistries. The basics of their functionality, however, are generally the same. All batteries include an anode, a cathode, an electrolyte, and a permeable separator between the electrodes. During charging, Li^+ ions generated from either the cathode or the electrolyte are

transported through the device and inserted into (intercalation) or adsorbed onto the anode. The discharging process is the opposite, whereby ions are extracted from (deintercalation) or spontaneously desorbed from the anode and move to the cathode. The movement of ions in the devices creates free electrons, which are then able to pass through the external circuit, generating the electrical current[66]. Through these mechanisms, energy is stored chemically.

Lithium-ion batteries are extensively used due to their high electrochemical performance. Their advantages include low self-discharge rates, high volumetric and gravimetric energy density, and high cell voltage. They do, however, present several issues. Due to their ageing process, lithium-ion batteries have relatively low power density, low theoretical capacity, sluggish kinetics, and poor life cycle stability [67]. Battery ageing is the process in which materials in the battery degrade over time, generally due to irreversible structural changes which result in a capacity decrease and power fading over time[68]. This can be due to several factors, including dendrite formation, swelling and shrinking of the electrode material over time upon charging and discharging, and unwanted reactions between the electrodes and the electrolyte. Ageing mechanisms occur at both the anode and cathode [68].

GQDs can be integrated into the anode or cathode of LiBs to improve device performance[69]–[74]. VO_2 can be used as a cathode in LiBs owing to its abundance, high capacity and low cost. Despite VO_2 possessing a high capacity compared to other cathode materials, its specific capacity is still much lower than that of common LiB anodes, thereby limiting the performance of the device. Furthermore, it suffers from fast capacity fading and poor high-rate performance. Therefore, Chao *et al.* [73] coated binder-free VO_2 nanobelts grown on graphene foam with GQDs to enhance their electrochemical properties. Functionalised GQDs were deposited on the surface of the VO_2 arrays via electrophoretic deposition. The measured specific capacity increased from 391 to 421 mAh/ g at 1/3 C upon GQD deposition. The GQDs homogeneously covered the surface of the nanobelts, acting as a structure regulator by preventing VO_2 agglomeration and minimising electrode damage during the cycling process, increasing the life cycle of the electrodes. Upon deposition of the GQDs, the cycle stability of the VO_2 electrodes improved from 85 to 94 % after 1500 cycles at 60 C. The increased number of active sites on the VO_2 electrodes due to the addition of the GQDs provides extra lithium-ion storage venues and increases the electron/ ion transport kinetics due to the increase in electrochemical activity.

MoS_2 is a promising anode material for LiBs. Its layered structure allows for Li^+ intercalation and provides numerous accessible active sites for ion storage. To reduce the limitations of MoS_2 resulting from internal pulverisation, poor rate capability and poor cycle stability, Guo *et al.* [74] doped the

material with hydrothermally synthesised GQDs via a solvothermal method. The GQDs enhanced ion transport, increased conductivity, regulated the structure during cycling, and widened the interlayer spacing in comparison to pristine MoS_2, promoting Li^+ intercalation. The cycle stability increased from 81 to 94 % after 80 cycles, and the capacity increased from 472 to 1099 mAh/ g at 0.1 A/ g upon GQD addition.

In all reports of GQD-modified electrodes for energy storage devices[52], [59]–[65], [69]–[74], *to the best of my knowledge, the edge shapes of the GQDs used are not mentioned*. For the reasons outlined in sections 1.1 and 1.2, knowledge of the edges of GQDs used as an electrode material is critical to the optimisation of the electrodes and device performance. The difference in the density of states and bandgap width resulting from the edge type will impact the extent to which the nanoparticles improve the device.

Additionally, it has been reported that pH conditions affect the quantum confinement of GQDs, with high pHs narrowing their bandgap and low pHs widening it[75]. This becomes a problem when considering the electrolyte to be used in the energy storage devices containing the nanoparticles. Since its pH will affect the conductivity and capacity of the electrode itself. Reports of device fabrication in the literature do not appear to consider this, and it therefore requires further investigation.

The aim of the project is thus to *identify the effects of edge shapes on the properties of GQDs and carbon fibre electrodes onto which GQDs have been deposited. Additionally, to investigate the impact of electrolyte selection on the energy storage capability of the carbon fibre electrodes*. To achieve this aim, GQDs were synthesised hydrothermally and electrochemically, and the effects of reaction conditions on their size, structure and properties were studied. GQDs with differing structures were deposited onto carbon fibre electrodes before analysing their surface and electrochemical properties.

3. Experimental

Triethanolamine (85 %) ($C_6H_{15}NO_3$), monosodium citrate ($NaC_6H_7O_7\cdot 2H_2O$) and sodium hydrogen carbonate ($NaHCO_3$) were purchased from Mistral Industrial Chemicals, Ltd. NI. Nitric acid (70 %) (HNO_3) was purchased from Thermo Fisher Scientific, Ltd. Sulfuric acid (1 M) (H_2SO_4) was purchased from Rapid Electronics, Ltd. Isopropyl alcohol ((CH_3)$_2$CHOH) was purchased from Sigma Aldrich. All chemicals used were of technical grade and were used as received. Carbon fibres (plain weave Pyrofil TR 30S 3K, 210 gsm, 300 μm thick) were obtained from EasyComposites. Graphite rods (70 mm length, 3 mm diameter, 99.9 % purity) were obtained from Redoxme and were HP-III grade. A platinum rod counter electrode (85mm length, 6mm diameter, platinum content 50 g/m^2 coated on type 2 titanium) was obtained from Spa Plating, Ltd. An Ag/ AgCl reference electrode (aqueous, filled with 3M saturated KCl) was obtained from Ossila, Ltd. A PTFE copper electrode holder (10x10 mm copper plate conductive substrate, PTFE body and gold-plated copper rod terminal) and an electrochemical cell (50 ml, borosilicate glass, PTFE lid) were obtained from Stonylab.

3.1. Hydrothermal synthesis of NGQDs

Nitrogen-doped GQDs were synthesised using a microwave-assisted hydrothermal method based on the work published by Ren *et al*.[76]. 2 g of sodium citrate were added to 12 ml of triethanolamine. The solution was stirred for 3 hours and was then placed in a domestic microwave oven (COMFEE, 700 W) at 33% power for times varying from 150 s to 195 s. After cooling, the resulting solutions were centrifuged at 8000 rpm for 15 mins, and the top layer was collected using a syringe for subsequent analysis and processing.

3.2. Electrochemical synthesis of N-GQDs

N-GQDs were synthesised by the electrochemical exfoliation of graphite rods. A modified version of the work by Ahirwar *et al*.[77] was used. Graphite rods were first heated at 200°C in an oven for 30 minutes, then manually exfoliated using an abrasive pad (grit number 150) to remove any external oxide layer formed upon cooling and washed with deionised water to remove any larger surface particles. 2 g of sodium citrate, 12 cm^3 triethanolamine and 25 cm^3 deionised water were added to an electrochemical cell. The solution was allowed to electrolyse for 20 minutes using a platinum and a nickel electrode by applying chronoamperometry at 10 V (VersaSTAT 3 Potentiostat Galvanostat). The graphite rods were then used as both the working and the counter electrodes, and chronoamperometry at 10 V was applied for 1 hour. The resulting solution was filtered through a 450 nm syringe filter to remove any graphite particles.

3.3. Deposition of GQDs on Carbon Fibre Electrodes

Electrophoretic deposition was used to attach N-GQDs to carbon fibres[78]. Carbon fibres were first prepared by ultrasonicating 0.5 g carbon fibres with 0.5 cm^3 of concentrated nitric acid for 10 minutes to increase hydrophilicity, followed by twice ultrasonicating with 0.5 cm^3 of deionised water for 10 minutes. The washed carbon fibres were screwed into a copper electrode holder. The carbon fibres in the electrode holder were used as the working electrode, and a platinum rod was used as the counter electrode in a 2-electrode half-cell with a GQD solution as the electrolyte (hydrothermally synthesised GQDs were diluted in a 60/ 40 ratio with deionised water, while electrochemically synthesised GQDs were used as made since the solution was already dilute). 10 V was applied to the cell using a DC power supply (Keithley 2200) for varied deposition times. The modified carbon fibres were removed from the cell and rinsed with deionised water for further testing.

3.4. Physical Characterisation

UV-Vis spectra of the N-GQD samples were measured using a UV-Vis spectrophotometer (Shimadzu UV-Vis UV 1800, 190-1100 nm scan range). The samples synthesised hydrothermally were diluted in a 1:50 ratio with deionised water. In contrast, the electrochemically synthesised GQDs were diluted in a 1: 20 ratio with deionised water to ensure all samples had a similar peak absorbance value. Samples were placed in a 3.5 ml UV quartz cuvette with a 1 cm path length and measured in a range of 190-700 nm.

Lateral size measurements of the GQDs were recorded using a transmission electron microscope (TEM) (JEOL JEM-2100). Hydrothermally synthesised samples were diluted in a 1:4 ratio with isopropyl alcohol (IPA), while electrochemically synthesised samples were diluted in a 1:2 ratio with IPA. Samples were drop cast (2 drops) onto 200 mesh carbon-coated copper grids, allowed to dry, and viewed under the TEM with acceleration voltage 200 kV at a resolution of 5 nm.

Crystallographic measurements of the GQDs were taken using X-ray diffraction (XRD) analysis (Bruker D8 Advance) with monochromatic CuKα radiation. Samples were drop cast onto a glass substrate and allowed to dry. Graphs were obtained between 10 and 90° (2θ) at 40 kV and 35 mA with a 0.02 °/s scan rate.

3.5. Electrochemical Characterisation

Electrochemical measurements were carried out in a 3-electrode half-cell configuration. Carbon fibres held in a copper electrode holder were used as the working electrode, a platinum rod was used as a counter electrode and an aqueous Ag/AgCl electrode was used as the reference. The

electrolyte used was 1 M H_2SO_4. Cyclic voltammetry, electrical impedance spectroscopy, open cell voltage and Mott Schottky plots were all measured using a potentiostat (VersaSTAT 3 Potentiostat Galvanostat).
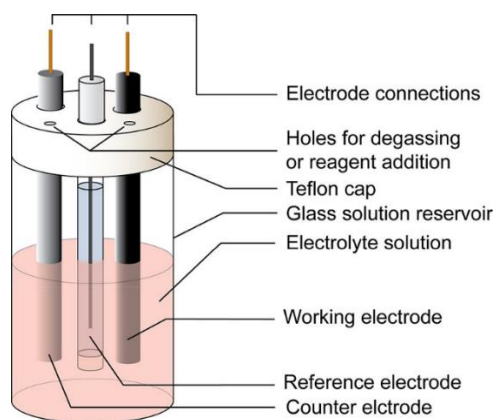

Figure 7:   *Schematic of a 3-electrode half-cell configuration*[79]

3.5.1.   Cyclic Voltammetry and Electrical Impedance Spectroscopy

Cyclic voltammetry (CV) was performed to confirm the presence of N-GQDs on the surface of the carbon fibres after electrodeposition and determine their energy storage capabilities. Scans used to calculate the specific capacitances of the electrodes were taken at 5 mV/s scan rate in a voltage window of -0.5 to 0.8 V with 1M H_2SO_4 as the electrolyte.

Cyclic Voltammetry measures the current in a cell when the applied voltage exceeds that predicted by the Nernst equation. The potential of the working electrode is measured against a reference electrode with a known constant potential. The voltage is swept (cycled) between two limit potentials, and the current that flows through the cell is plotted. It is commonly used as a tool to investigate electron transfer reactions through oxidation and reduction processes[79]. A standard cyclic voltammogram is displayed in *Figure 8*.
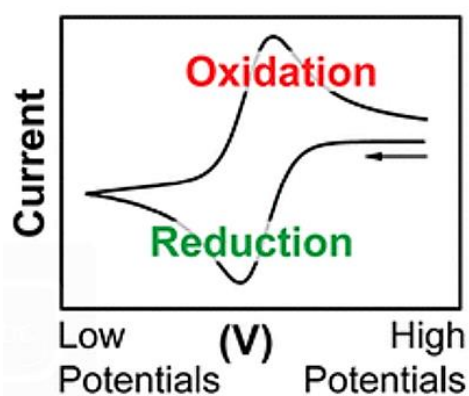

Figure 8:   *Standard shape of a cyclic voltammogram displaying the peak representations*[79]

The specific capacitance (C_s) of the working electrode at a given scan rate can be determined by:

$$C_s = \frac{\int I \ dV}{2vm\Delta V} \qquad (8)$$

where $\int I \ dV$ is the closed polygon area of the voltammogram, v is the scan rate, m is the mass of the electrode, and ΔV is the potential range [80].

Electrochemical measurements were conducted on unmodified and modified carbon fibre electrodes. One modified carbon fibre electrode had hydrothermally synthesised GQDs deposited, while the other had electrochemically synthesised GQDs deposited. The double layer capacitance was separated, i.e. deconvoluted from the total capacitance, by calculating the values separately from pseudocapacitive and quantum capacitive contributions for each electrode by following a method by Morales and Risch[81].

To accurately determine the double layer capacitance, it is important only to investigate the regions in which pseudocapacitive contributions are negligible. Faradaic reactions have relatively slow kinetics; therefore, lower scan speeds are necessary to provide time for oxidation and reduction reactions. Cyclic voltammograms recorded at low scan speeds can thus provide a window between the reduction and oxidation peaks in which no pseudocapacitive reactions can interfere with total capacitance measurements. Therefore, cyclic voltammograms were obtained between -0.5 V and 1.2 V at slow scan speeds (1 mV/s – 10 mV/ s) with a 1M H_2SO_4 electrolyte to determine the voltage range in which redox reactions do not occur.
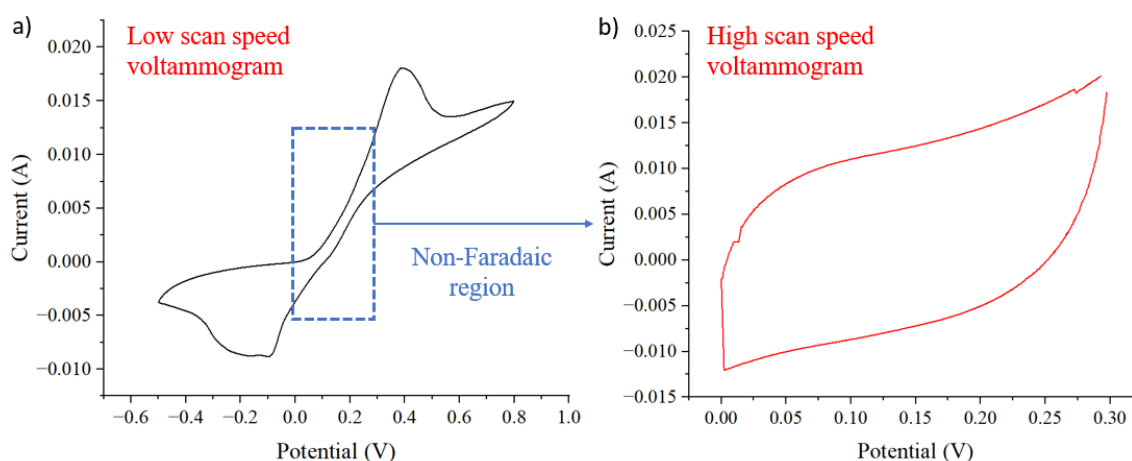

Figure 9: *Cyclic voltammograms of electrochemically synthesised N-GQDs: a) between -0.5 V and 1.2 V at a scan speed of 0.005 V/s. The non-Faradaic region is highlighted, and b) between 0 V and 0.3 V at a scan speed of 1 V/s. The rectangular shape of the voltammogram is indicative of purely double layer capacitance.*

Performing CV at high scan speeds ensures no charge transfer reactions can occur, even if the window determined through the method above has been slightly miscalculated. It should be noted that the window should contain the open circuit potential for the electrode. Voltammograms at higher scan speeds (0.5 V/s – 1 V/s) limited to the voltage window in which Faradaic reactions are negligible (0 V – 0.3 V) were thus produced to view the purely double layer contribution to capacitance (*Figure 9*).

Voltammograms were adjusted by eliminating the contribution of unmodified carbon fibre electrodes to the capacitance measurements, so all results reflect only the GQDs. iR errors were then determined. The potentiostat is able to compensate for any resistance between the working and counter electrode; however it is unable to compensate for resistance encountered between the working and reference electrode. Since the measurement between the working and reference electrode is the the potential difference of interest, it is necessary to adjust the electrochemical measurements to negate the associated error. The potential difference of interest ($V_{important}$) can be determined from the equation:

$$V_{important} = V_{measured} - I_{cell} \cdot R_u - V_{oc} \tag{9}$$

where $V_{measured}$ is the voltage measured by cyclic voltammetry, I_{cell} is the measured current, V_{OC} is the open circuit potential, which is measured using the potentiostat, and R_u is the uncompensated resistance. R_u can be determined from the EIS bode representations of the electrical impedance spectroscopy measurements. Nyquist plots were recorded at a frequency range of 50 mHz - 10 kHz at 10 points per decade with an alternating current amplitude of 10 mV RMS and a DC potential of 0.15 V (since it is at the centre of the measured potential range). The bode plots displayed a negative gradient before reaching a flat baseline (i.e. a gradient of zero) starting at ~1000 Hz. For frequency values falling on this baseline, the measured impedance is R_u. The value of R_u was thus taken to be the measured impedance at 10 kHz. Open cell potential for the electrochemically synthesised and hydrothermally synthesised GQD electrodes were found to be 88.6 mV and 90.2 mV, respectively. R_u for the electrochemically synthesised GQDs was 1.46 Ω, and 1.01 Ω for the hydrothermally synthesised GQDs.

To determine the double layer capacitance for the GQDs, graphs were plotted of current against scan rate for currents at the open circuit potential (i.e. corrected values of the current obtained at the open circuit potentials for the electrodes at scan speeds of 0.5 V/s – 1 V/s) and the best fit lines were determined. The best fit lines were found to be power functions, and their gradients are the C_{dl} for each electrode. The indices in the fitting equations were found to be close to 1, suggesting the determined double layer capacitive values were reasonably valid.

Mott Schottky analysis was conducted between -0.5 and 0.8 V at 100 Hz. Flat band potential can be obtained from Mott Schottky analysis by extrapolating a linear line of best fit to the x-axis.

3.5.2. Bandgap Determination

Optical bandgap calculations were conducted by graphing Tauc plots using measured UV-Vis data. The Tauc method is based on the equation:

$$(\alpha \cdot hv)^{\frac{1}{\gamma}} = B(hv - E_g) \tag{10}$$

where α is the absorption coefficient for the sample, h is Planck's constant, v is the photon frequency, B is a constant of proportionality, E_g is the bandgap energy and γ is equal to ½ for a direct bandgap transition, or 2 for an indirect bandgap transition [82].

To obtain the absorption coefficient, the concentration of aqueous samples is required, and the coefficient is calculated based on the Beer-Lambert law:

$$A = \varepsilon b C \tag{11}$$

where A is the absorbance, ε is the molar absorbance coefficient, b is the path length, and C is the sample concentration [83]. The molar absorption coefficient and molar absorbance coefficient are related by the equation:

$$\alpha = \frac{4\pi\varepsilon}{\lambda} \tag{12}$$

[84]. It has previously been demonstrated that nitrogen-enriched carbonaceous quantum dots possess adsorbed anionic water clusters ($[OH(H_2O)_n]^-$) on their surface in solution[85], which will therefore affect the bandgap of the nanoparticles due to changes in size/ surface area of the particles upon their addition. Since all other structural and electrochemical testing was conducted in solution, either diluted or with an aqueous electrolyte, drying the samples to determine their concentration was not worthwhile since the absence of water clusters will alter their structure. It was instead decided to estimate the absorption coefficient by diluting samples relative to each other and plotting a graph of the peak absorption coefficient against relative concentration for each sample. A linear best fit line was then plotted, and its slope was determined. The slope of this line is equal to the product of the extinction coefficient and path length. The path length for the UV-Vis measurements was 1 cm.

Based on these approximated absorption coefficients, Tauc plots were graphed of $(\alpha \cdot hv)^{\frac{1}{\gamma}}$ against hv, where v is determined from the standard equation:

$$v = \frac{c}{\lambda} \tag{13}$$

with *c* the speed of light and the wavelength, *λ*, obtained directly from the UV-Vis plots. Graphs were plotted for both *γ* equal to ½ and 2 to determine if the bandgap transitions are direct or indirect for the nanoparticles. The linear part of the graph was subsequently fitted with a straight line, and the equation was determined. The best fit line was then extrapolated down to the x-axis. The point at which the best fit line intercepts the x-axis gives the bandgap value, shown in *Figure 10*.
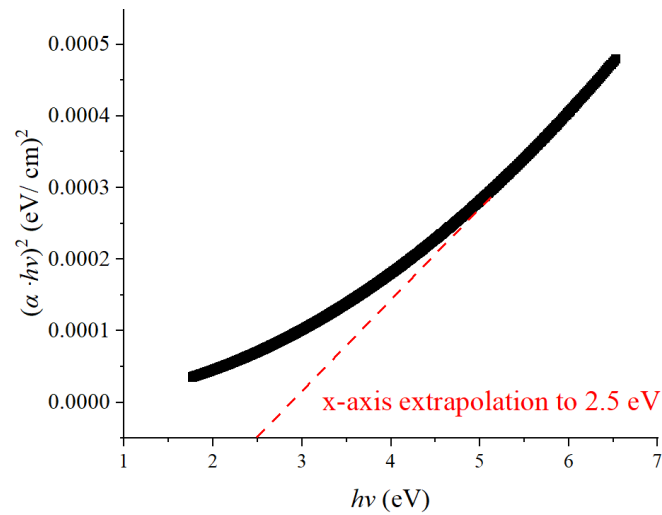
Figure 10: *Tauc plot of hydrothermally synthesised N-GQDs. The linear part of the plot is extrapolated to 2.5 eV, which is equal to the bandgap.*

From these plots, the bandgap for all GQDs was determined to be direct (as plots for indirect bandgap transitions resulted in negative bandgap values). This agrees with previously simulated data demonstrated through density functional theory (DFT) calculations that all GQDs displayed a direct bandgap transition [86].

4.   Results and Discussion

4.1. Hydrothermal Synthesis of N-GQDs

A synthetic method to produce doped GQDs was selected over pristine GQD synthesis for the reasons outlined in section 2.4. Nitrogen-doped GQDs were specifically chosen as nitrogen is more electronegative than carbon and is an electron acceptor, thereby attracting electrons from the electrolyte, and improving electrochemical performance. Furthermore, the difference in electronegativity leads to improved wettability of the nanoparticles, decreases work function and leads to higher surface energy. The additional atoms increase the surface area of the nanoparticles, providing a larger area on which the electrical double layer can form, increasing their energy storage potential[87].

The introduction of nitrogen through doping introduces defect energy levels which serve to decrease the HOMO-LUMO gap in GQDs. This results from the hybridisation of the p_z orbitals of N and C atoms. The π bonds in N-GQDs have a lower energy of formation than σ bonds, and therefore their formation contributes to decreasing the bandgap [88].
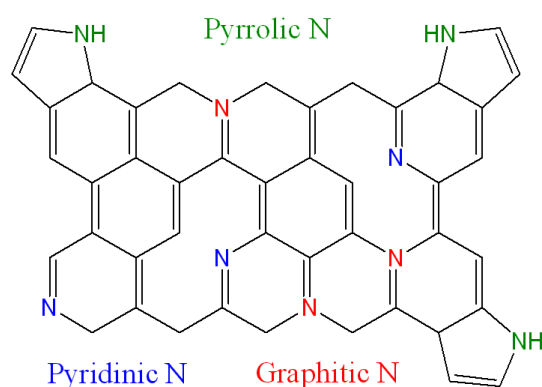
Figure 11*:   A nitrogen-doped GQD demonstrating the different configurations the doped N atoms can take (pyrrolic, pyridinic or graphitic).*

The configurations of the C-N bonds in the GQDs will play a role in the energy storage capability of the N-GQDs. The possible configurations are pyrrolic nitrogen, pyridinic nitrogen and graphitic nitrogen, shown in *Figure 11*. All configurations introduce midgap states to the bandgap[89]. Pyridinic and pyrrolic nitrogen lead primarily to pseudocapacitive energy storage in the N-GQDs, while graphitic nitrogen can enhance conductivity resulting from electronic couplings between carbon and nitrogen, which is favourable for electron transport in the nanoparticles[40]. Pyrrolic nitrogen has previously been shown to increase the density of states of the GQDs to the greatest extent, thereby reducing the limiting effects of quantum capacitance the most effectively[39]. Nitrogen groups can also be present on the nanoparticles as amine groups functionalised on the

edges or basal plane. These groups will further increase specific capacitance as they are highly ionisable and contribute to Faradaic energy storage[90].

There are two types of approach to synthesising GQDs, namely top-down synthesis and bottom-up synthesis. Top-down synthesis involves the cutting and exfoliation of larger, readily available carbon sources, while bottom-up synthesis synthesises the quantum dots from smaller carbon-containing compounds[91].

The microwave-assisted hydrothermal synthesis of GQDs from monosodium citrate and triethanolamine is a bottom-up synthetic technique. The rapid microwave heating leads to pyrolysis of the precursor molecules. At high temperatures, condensation and esterification occur between the hydroxyl and carboxylic acid groups on neighbouring precursor molecules, followed by aromatisation through aldol condensation and cycloaddition reactions. When a critical point of the concentration aromatic clusters in the reaction mixture has been reached, a burst nucleation occurs, forming N-GQDs. Triethanolamine is both a solvent and a nitrogen source in the reaction[20].
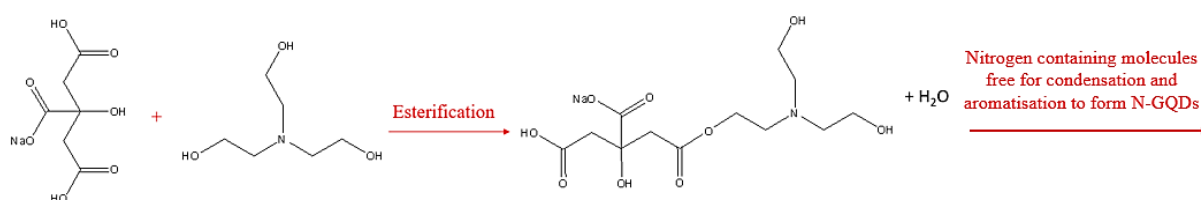

Figure 12: *Part of the mechanism for the synthesis of N-GQDs from sodium citrate and triethanolamine. The scheme displays an esterification mechanism between sodium citrate and triethanolamine, demonstrating how nitrogen doping of the GQDs takes place. The ester molecules are now free to react further to form GQDs.*

A microwave power setting of 33% was found to result in the most controllable synthesis. A lower (10 %) power setting resulted in the formation of a dilute solution of N-GQDs, and a large amount of sodium citrate residue remained. It is assumed that the microwave irradiation did not heat the solution rapidly enough, or to a high enough temperature, to dehydrate a sufficiently large quantity of precursor citrate molecules to allow the formation of many N-GQDs. A higher (100 %) power setting resulted in the formation of a solid substance, presumed to be graphene oxide, as the higher temperatures allowed for extensive aromatisation and agglomeration of the nanoparticles. It has previously been shown that graphene oxide can be formed via microwave irradiation from graphite particles[92], and a similar mechanism is thought to have occurred here; however further characterisation would be necessary to confirm this.

Varied irradiation times were tested (150 s, 165 s, 180 s and 195 s). All reactions were conducted with the precursor solutions placed in the centre of the microwave, and the heating was continuous for the entire reaction duration. From here on, N-GQDs synthesised hydrothermally for varying reaction times will be referred to as HT1, HT2, HT3 and HT4 for reaction times 150 s, 165 s, 180 s, and 195 s, respectively. The literature reports the formation of a pale-yellow solution of the reaction mixture, indicating the formation of N-GQDs[76]. It was observed that a pale-yellow solution was formed for HT1, and the solutions darkened upon increasing reaction time (*Figure 13*). Samples were illuminated with a 395 nm UV torch upon synthesis to confirm the presence of fluorescence.
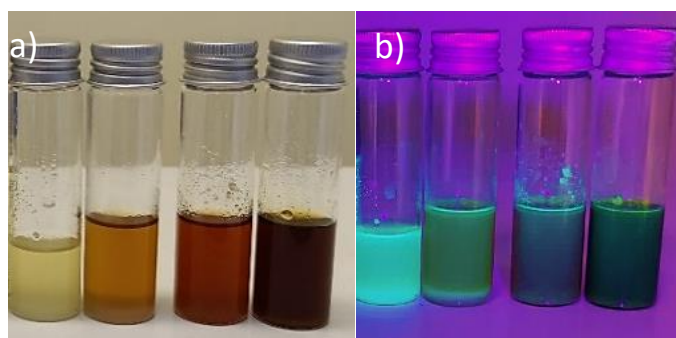

Figure 13: *HT1-4 (from left to right) a) under standard lighting and b) under a 395 nm UV torch.*

XRD analysis was carried out for each solution to confirm the presence of graphetisation and crystallinity in the structures. The XRD graph of sample HT1 (*Figure 14a*) displayed a diffraction peak at 2θ = 23.89° due to the C (002) crystal plane index, indicative of an aromatic structure with a high degree of parallel and azimuthal orientation, thus confirming the structure is graphene. The unsymmetrical nature of the peak suggests the presence of aliphatic structures doped on the surface of the N-GQDs, as was expected due to the introduction of nitrogen and oxygen-containing groups during synthesis. Furthermore, the diffraction peak corresponds to a d_{002} spacing of 0.37 nm. This is slightly larger than the interlayer spacing of graphite (0.334 nm); however this increase can be attributed to the presence of functional groups on the basal plane, forcing the graphene layers further apart[93].

The smaller peak at 2θ = 37.34° corresponds to the d_{100} plane index. This represents the length of the unit cell and is equivalent to 0.24 nm, close to the d_{100} spacing in graphite (0.246 nm), further emphasising the graphitic nature of the nanoparticles[94].

The XRD graphs for samples HT2-4 were extremely similar to that for HT1. The XRD graph for sample HT4 is displayed in *Figure 14b* for comparison. The sample has identical d_{002} and d_{100} spacing as the other samples, with the only difference being the increase in intensity of the peaks, along with the peaks being slightly wider which is a result of the larger size of the nanoparticles in the sample[95].
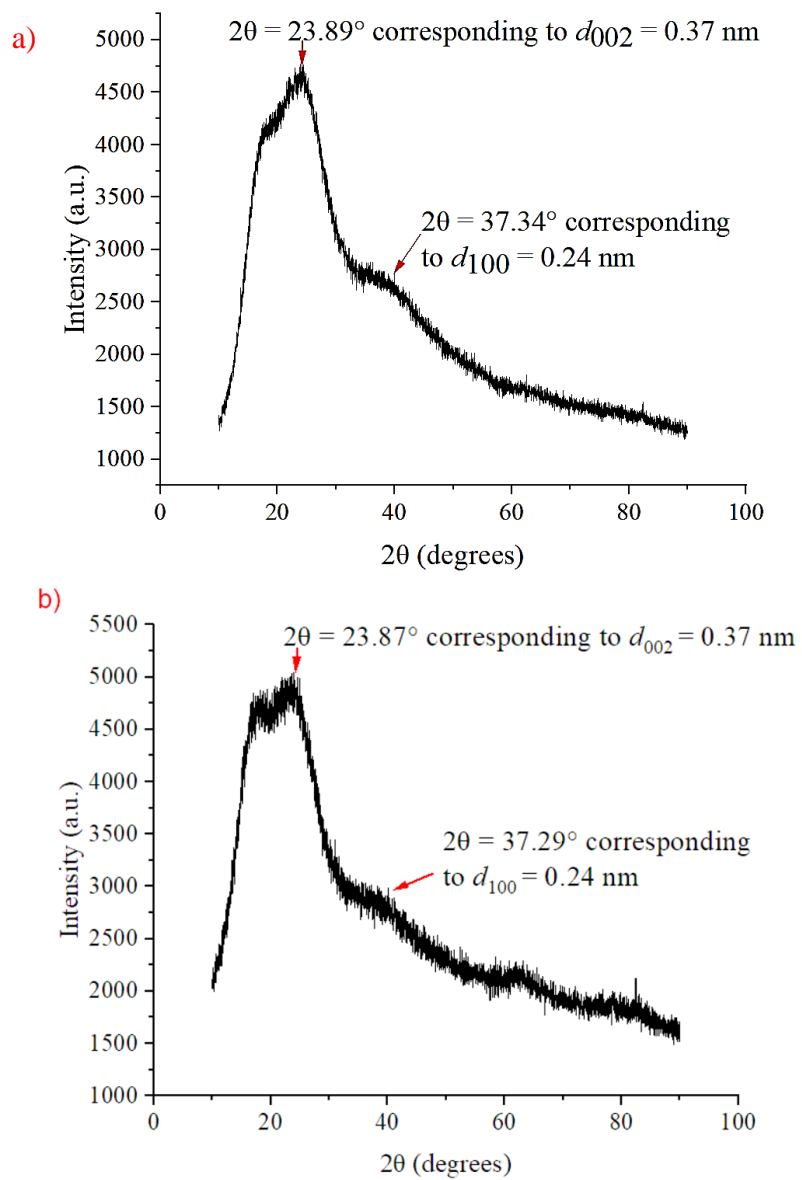
Figure 14: *XRD graph of hydrothermally synthesised N-GQDs a) sample HT1) and b) sample HT4*
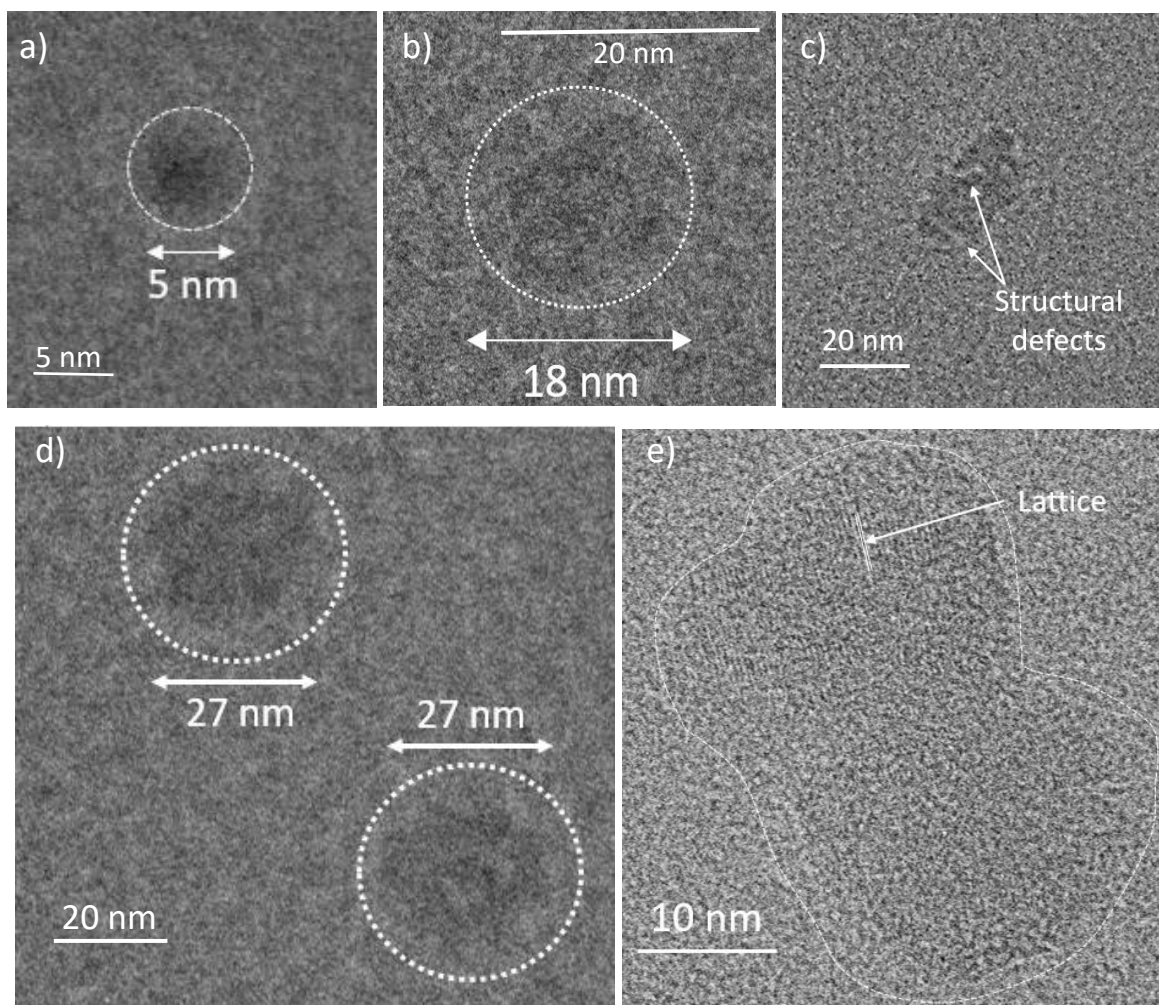
Figure 15: *TEM images of GQD grown via hydrothermal synthesis a) HT1; b) HT2; c) HT3 displaying structural defects; d) HT3 and e) HT4 with a visible lattice structure.*

TEM images (*Figure 15*) show an increase in the lateral dimension of the GQD size upon increased microwave reaction time (~ 5 nm for HT1, ~ 18 nm for HT2, ~27 nm for HT3, ~40 nm for HT4). More than 15 GQDs were imaged per sample using TEM, all displaying similar lateral sizes. HRTEM should be carried out for complete size distribution analysis in the future. It should, however, be noted that the shapes of the nanoparticles were considerably less uniform for HT4 compared with the smaller nanoparticle sizes. For smaller nanoparticles, the overall shape was generally relatively circular, but for HT4 some particles were somewhat ovular/ oblong-shaped. This is likely due to the increased reaction times resulting in the aggregation of multiple nanoparticles in one plane (i.e. all attached vertically or horizontally).

The larger size of the nanoparticles upon increasing reaction times is supported by spectra obtained through UV-Vis (*Figure 16*). The redshift seen in the spectra indicates a narrowing of the bandgap, which is expected as particle size increases. The particles likely increased in size upon increasing

reaction as the longer heating times allowed more dehydration reactions to occur, enlarging the synthesised quantum dots[96].

The peaks between 219 and 233 nm are a result of the π-π* transition in C=C, and the peaks at ~270 nm are due to the π-π* transition in C=N[93], indicating that the nanoparticles have been successfully doped with nitrogen. The nitrogen peak is most prominent in HT1, suggesting that these particles had the largest ratio of nitrogen present in their structure.
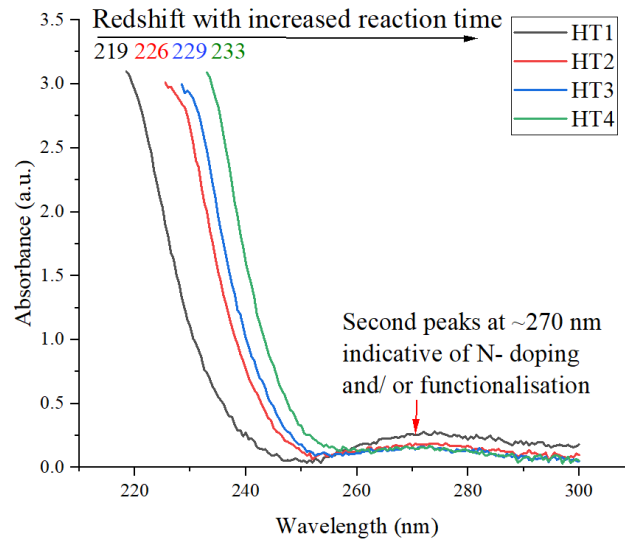
Figure 16: *Effect of the reaction time on the UV-Vis spectra of N-GQDs showing the peak positions of interest, which result from C=C bonds. The peaks at ~270 nm are a result of N- bonds in the molecules, confirming the presence of nitrogen in the N-GQDs.*

The size of the optical bandgaps was determined from the UV-Vis spectra by Tauc plots. The bandgaps for HT1-4 were 2.50, 2.18, 2.12 and 2.06 eV, respectively. These values are within the reported bandgap ranges for GQDs[97]. Furthermore, these values confirm that the redshift seen in the UV-Vis spectra is representative of a narrowing of the bandgap upon increasing particle size. This is due to a weakening of the quantum confinement effect upon increasing nanoparticle size as a larger number of atomic orbitals are involved in bonding in the particles, decreasing the distance between the empty and filled states and thus decreasing the bandgap.

Semiconductor quantum dots are typically modelled by the Brus equation, where the bandgap energy is given by:

$$E_{g(qd)} = E_{bulk} + \frac{h^2}{8R^2}\left(\frac{1}{m^*_e} + \frac{1}{m^*_h}\right) - \frac{1.8e^2}{4\pi\varepsilon_0\varepsilon_r R^2} \tag{14}$$

Here, $E_{g(qd)}$ is the bandgap energy of the quantum dot, E_{bulk} is the bandgap energy for the bulk material, R is the radius of the quantum dot (or alternatively the length of its edges, if it is not

round), m^*_e and m^*_h are the relative mass of an excited electron and a hole, respectively, ε_0 is the permittivity of a vacuum, and ε_r is the relative permittivity[98]. The second term in the equation represents the confinement energy, and it can be seen from this that $E_{g(qd)}$ is inversely proportional to the square of the radius of the nanoparticle.

Graphene quantum dots, however, do not follow this relation. Due to the Dirac like quasiparticles in graphene, the energy gap instead follows the relation:

$$E_{\text{gap}} \propto \frac{1}{L} \tag{15}$$

with L the length of its edges[99]. This is an expected trend for confined Dirac fermions due to the correlation shown in equation (16).

$$E_{\text{gap}} \propto k_{\text{min}} \approx \frac{2\pi}{L} \tag{16}$$

where k_{min} is the minimum Fermi wavenumber[16]. This relation is equivalent to that shown in equation (2), since the length an edge of the GQD is directly proportional to the square root of the total number of atoms in the quantum dot. This is easiest to see from a basic example; *Figure 17* shows three simple GQDs of increasing dimensions. Using the d_{100} spacing obtained from the XRD measurements (*Figure 14*) (0.24 nm), the dimensions of each particle can be obtained. For ease, it is assumed each edge is passivated with a hydrogen atom. It can be seen from *Figure 18* that a linear relationship exists between L and $\sqrt{N}$ with an R^2 coefficient is 0.9974, where the value is slightly less than 1, likely arising from the standard experimental error in calculating the d_{100} spacing. This therefore confirms that both equations are equivalent for GQDs.
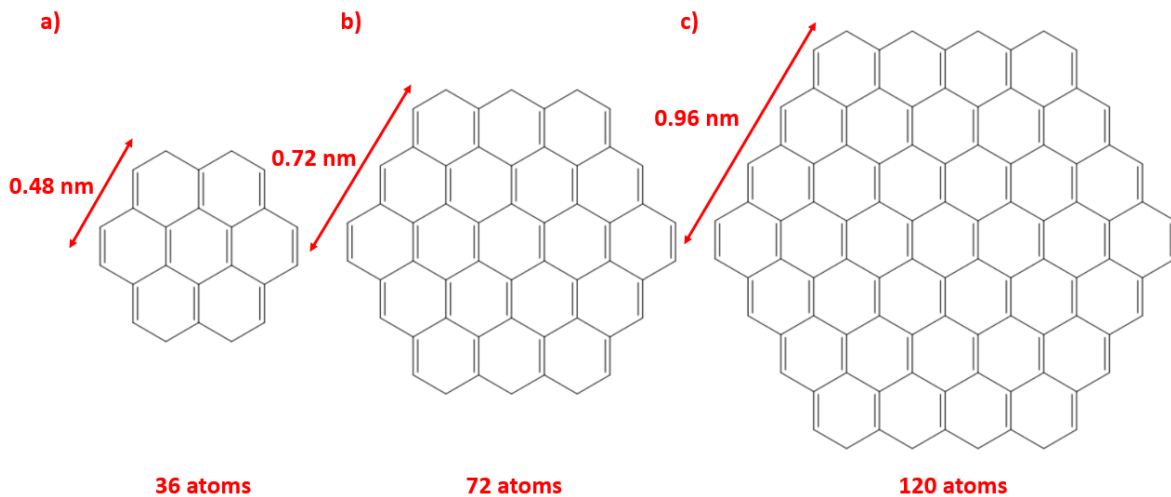
Figure 17: *Basic examples of zigzag GQDs. The length of each side was calculated based off XRD d_{100} spacing obtained from the this work (0.24 nm). The calculated number of atoms includes the total number of carbon and hydrogen atoms, where hydrogen atoms are assumed to passivate each edge.*
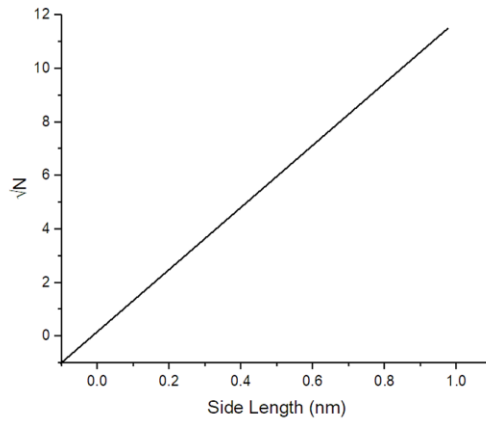
Figure 18: *Graph showing the correlation between L and $\sqrt{N}$ for the GQD examples shown in Figure 17. The R^2 coefficient is 0.9974, demonstrating the strong linear relationship between the variables.*

Table 1: *Comparison of hydrothermally synthesised GQDs. Samples HT1-4 were synthesised in this work and are described above, while the final three samples are data obtained from literature.*

Sample name	Synthesis method/ time	Particle size/ nm	Bandgap/ eV
HT1	Hydrothermal (microwave) 150 s	5	2.50
HT2	Hydrothermal (microwave) 165 s	18	2.18
HT3	Hydrothermal (microwave) 180 s	27	2.12
HT4	Hydrothermal (microwave) 195 s	40	2.06
N-GQDs derived from coal [100]	Reflux 24 hours followed by N doping via a solvothermal technique	5.86	2.05
N-GQDs derived from sucrose [101]	Reflux 8 hours	3.5	3.09
N-GQDs derived from graphene oxide [102]	Hydrothermal (autoclave) 10 hours	3.2	2.36
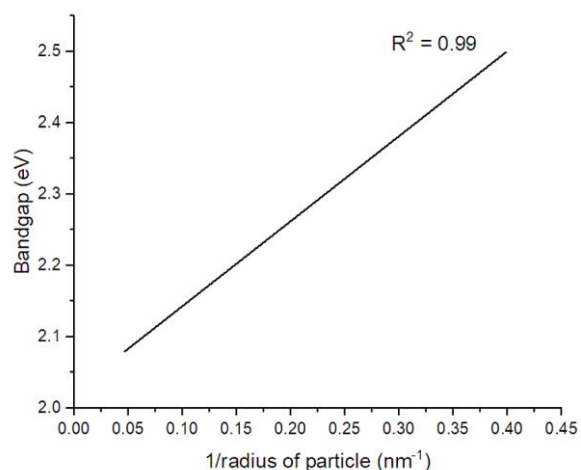
Figure 19: *Graph of bandgap vs. 1/ radius of the nanoparticle for samples HT1-4, showing the strong linear relationship between the two variables.*

The bandgaps obtained for HT1-4 are plotted in *Figure 19*. The particles are assumed to be spherical and so the radius of the GQDs are used in place of the length of an edge. The results display the expected a linear correlation between 1/R and the measured energy gap outlined in equation (15). However, the relationship is not directly proportional since the best fit line will not pass through (0,0). This is unsurprising since GQDs are particles with a lateral dimension of less than 100 nm, with the minimum bandgap of an N-GQD being approximately 1.9 – 2.1 eV[19], depending on doping quantities (i.e., 1/R will measure a minimum of 0.02 nm^{-1} and the minimum bandgap will be 1.9 – 2.1 eV, so the best fit line will therefore never pass through (0,0)).

It should be noted that the final three samples in Table 1 do not fit this correlation when compared to the samples synthesised in this work and have not been included in the graph. This is due to the influence of the synthetic route utilised on the bandgap[103], meaning the correlation coefficient in the bandgap relation will differ depending on the synthetic technique used. This is primarily due to the effect of the synthetic method on the quantity of doped and functionalised atoms on the nanoparticles. The examples are only included in the table for comparative purposes of bandgap sizes.

4.2. Electrodeposition of N-GQDs on Carbon Fibres

It has previously been reported by Liu *et al.*[104] that smaller GQDs display higher rate capability and faster frequency response times than larger GQDs. Smaller nanoparticles result in shorter ion diffusion distances and therefore shorter ion diffusion times. Smaller GQDs also possess a higher surface area to volume ratio, increasing the surface area of the electrodes to a greater extent than larger nanoparticles and providing a greater area upon which the electrical double layer can form. Although smaller nanoparticle size results in a wider HOMO-LUMO gap which can negatively affect

specific capacitance, the doping of GQDs with nitrogen narrows the bandgap and provides a Faradaic energy storage component to the specific capacitance, therefore mitigating some of the adverse effects to capacitance. For these reasons, the GQDs with the smallest particle size (HT1) were selected for initial capacitance testing.

Cyclic voltammetry was carried out on carbon fibres with N-GQDs electrodeposited for various times (10 min, 20 min, 30 min, 40 min, 50 min, and 60 min). The specific capacitances of electrodes with each deposition time were calculated from the CV curves using equation (8). It was found that the ideal deposition time was 30 minutes; shorter times resulted in fewer deposited GQDs and therefore the specific capacitances of the doped carbon fibre electrodes were lower, while at longer deposition times the deposited N-GQDs began to agglomerate on the surface of the fibres, lowering the surface area of the GQDs and consequently reducing the capacitance.

Cyclic voltammetry was carried out on carbon fibres with HT1 particles electrodeposited (*Figure 20*). The voltammogram displayed an (expected) increase in redox peaks due to the oxygen and nitrogen groups on the N-GQDs. The specific capacitances of the unmodified, pretreated-only, and CFs with electrodeposited N-GQDs were 16, 37 and 60 F/g, respectively, showing a 275 % increase in the specific capacitance between the unmodified fibres and the fibres with N-GQDs deposited. It is worth noting that the increase in specific capacitance for the pretreated-only CFs is due to the Faradaic reactions occurring due to the addition of oxygen groups to their surface by ultrasonication in concentrated nitric acid. Some redox peaks are also visible on the voltammogram of neat carbon fibres. This is a result of a small pre-existing oxide layer on the surface of the fibres since the voltammograms could not be produced in an inert atmosphere and were therefore all conducted at atmospheric pressure (in the presence of oxygen).
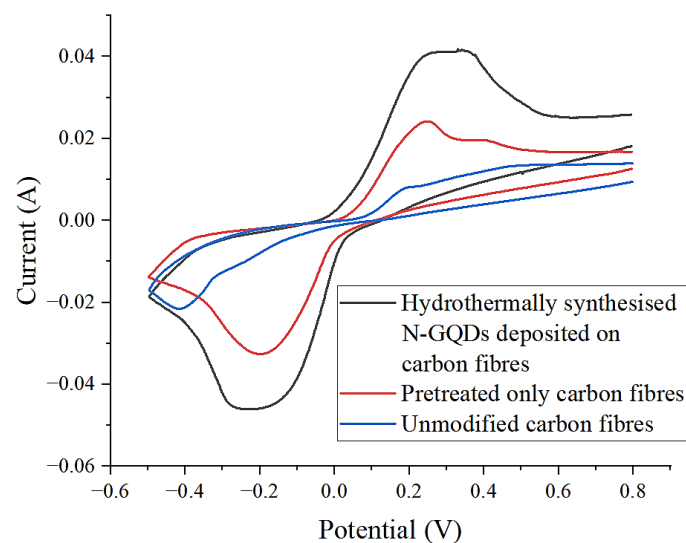
Figure 20: *Cyclic voltammograms at 5 mV/s of unmodified carbon fibres (blue), pretreated carbon fibres (red) and carbon fibres with N-GQDs (HT1) electrodeposited (black) in 1M H_2SO_4 electrolyte*

The addition of GQDs to carbon-based electrodes has been investigated in the literature. As described in section 2.6.1., GQDs were embedded into activated carbon electrodes. The activated carbon electrodes (without GQDs) had a specific capacitance of 246 F/g, and the activated carbon electrodes with interspersed GQDs had a specific capacitance of 388 F/g[63], a 58 % increase in specific capacitance. Tjandra *et al.* [78] electrodeposited GQDs on the surface of carbon cloth and reported a specific capacitance of 70.7 mF/g for the GQD-enhanced electrode. The value of the specific capacitance of neat carbon cloth was not reported in the paper, but has been found to be 1-2 mF/g in other work[105]. The carbon cloth therefore displayed an increase in specific capacitance of ~70%. Chen *et al.*[106] hydrothermally embedded GQDs into 3D graphene electrodes and reported a 97 % increase in specific capacitance of the electrodes upon GQD addition.

The more significant increase in specific capacitance displayed in this work can be partially attributed to the nitrogen doping of the GQDs used here, as the nitrogen present increases pseudocapacitance of the nanoparticles and the literature results outlined above integrated undoped GQDs. Increases in specific capacitances close to that reported in this work have been reported for other (non-carbon based) electrodes upon doped GQD addition. Sulfur and nitrogen co-doped GQDs were embedded into polyaniline electrodes. The specific capacitance was reported to increase from 177 F/g for pristine polyaniline electrodes to 645 F/g upon GQD integration[65], a 264 % increase. It is also worth considering that the inability to conduct cyclic voltammetry in an inert environment likely also increased the measured specific capacitances in this work due to reactions with atmospheric oxygen and may be a cause for the large increase in specific capacitance.

Table 2: *Comparisons of percentage increase in specific capacitance of electrodes modified by the addition of GQDs. Increase in specific capacitance is the increase in specific capacitance between unmodified electrodes and the electrodes with integrated GQDs.*

Electrode Material	Electrolyte	Scan Speed/ Current Density	Increase in Specific Capacitance/ %	Ref
N-GQDs/ carbon fibres	1M H_2SO_4	5 mV/s	275	This work
GQDs/ activated carbon	6M KOH	1 A/g	58	[63]
GQDs/ carbon cloth	1M H_2SO_4	50 mV/s	70	[78]
GQDs/ 3D graphene	1M H_2SO_4	1.25 A/g	97	[106]
S-N-GQDs/ polyaniline	1M H_2SO_4	0.5 A/g	264	[65]

4.3. Electrochemical Synthesis of N-GQDs

The electrochemical synthesis of N-GQDs from graphite rods is a top-down synthetic method. The method proposed by Ahirwar e*t al*. [77] begins by exposing graphite rods to high temperatures to create surface defects. While equipment restrictions did not allow for heating temperatures of the graphite rods to be as high as in this method, which used a heating temperature of 1050°C for 5 minutes, the heating of the graphite rods to 200°C for 30 minutes is assumed to have created surface defects in the graphite. It has been shown that graphene oxide can be simultaneously reduced and oxidised under temperatures as low as 95 °C, i.e., its structure can be altered at low temperatures[107], and, while further investigation would be required to confirm, the results suggest that structural defects could occur at 200 °C in graphite rods. Regardless of whether this is the case, Hossain and Wang [108] exfoliated graphite rods at room temperature without first inducing defects, and therefore heating the rods was not necessary, though it may have reduced the reaction time required.

The electrolyte for the reaction was a solution of sodium citrate, triethanolamine and water since utilising the same reagents for both the hydrothermal and electrochemical GQD synthesis was likely to create comparable GQDs across synthetic methods, particularly ensuring triethanolamine is present in both reactions since a nitrogen source is required to synthesise N-GQDs. The decision was made to electrolyse the electrolyte solution before its use in the synthesis of GQDs to induce more hydroxyl ions in the solution. Typical electrochemical synthesis of GQDs employs dilute NaOH as an electrolyte due to its easy dissociation, resulting in high availability of OH^- ions. Since dissociation of triethanolamine and sodium citrate into free OH^- ions is unlikely under the reaction conditions used, the electrolysis of water before the reaction began introduced a sufficient quantity of ions to the electrolyte.

When a potential is applied to the graphite rod electrodes in the electrolyte, the OH^- ions oxidise on the defect sites on the surface of the graphite rod, producing oxygen which then forces the graphite layers apart. Further ions then intercalate between the layers, widening the layer spacing further. The electric field cleaves the C=C bonds, and ultimately the graphite rods are electrochemically exfoliated, forming GQDs [77].
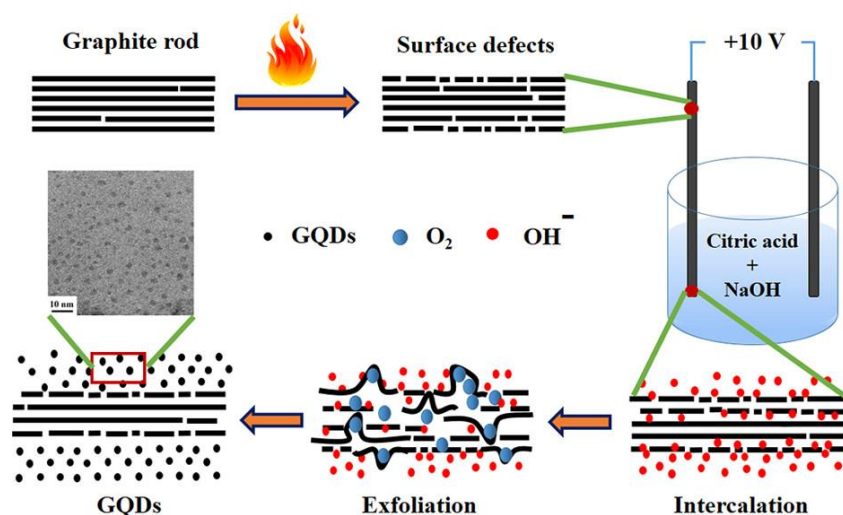
Figure 21*: Mechanism of the electrochemical synthesis of GQDs conducted by Ahirwar et al. [77]. The synthesis used was very similar to this and proceeded via the same mechanism, but the electrolyte solution was composed of sodium citrate, water and triethanolamine instead of citric acid and sodium hydroxide.*

The UV-Vis spectrum of EC1 is shown in *Figure 22*. The peak at 243 nm is a result of the π-π* transition in C=C, and the peak at 270 nm is due to the π-π* transition in C=N, indicating that the nanoparticles have been successfully doped with nitrogen[93]. From the Tauc plot, the bandgap for EC1 was found to be 3.01 eV. This bandgap is within the expected range for N-GQDs and will be discussed in relation to the UV-Vis spectra of hydrothermally synthesised GQDs in section 4.4.

Figure 22*: UV-Vis spectrum of sample EC1. The peak at 243 nm results from C=C bonds. The peak at ~270 nm is a result of N- bonds in the molecules, confirming the presence of nitrogen in the N-GQDs.*

TEM images of the electrochemically synthesised N-GQDs were taken and are displayed in *Figure 23*. The TEM images showed that the average size of the nanoparticles was 6 nm, meaning they are a comparable size to HT1 nanoparticles and will be compared directly against them. There was a small amount more variability in the dimensions of EC1 nanoparticles than HT1, but all nanoparticles seen on the TEM were found to be between 5 nm and 7 nm.

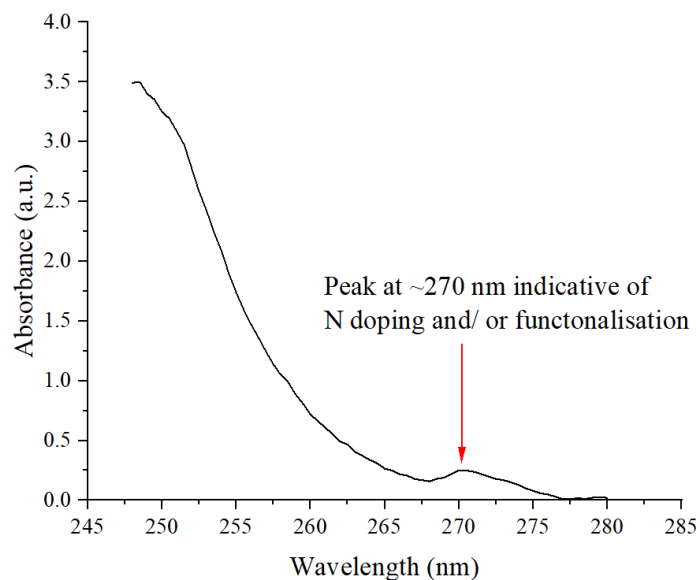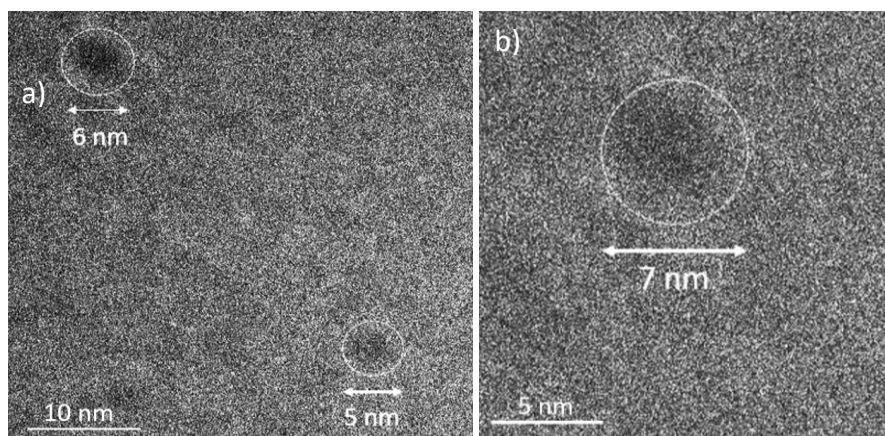*Figure 23: TEM images of sample EC1. The sample showed increased polydispersity compared to hydrothermally synthesised GQD samples, and the average size was 6 nm.*

It should be noted that the electrochemical synthesis was less controllable than the hydrothermal synthesis; altering the reaction time did not affect the size of the electrochemically synthesised nanoparticles. Longer reaction times produced a more concentrated solution of nanoparticles but had no noticeable impact on their structure. For this reason, only samples HT1 and EC1 will be compared.

XRD analysis of the electrochemically synthesised N-GQDs (EC1) was carried out. The XRD graph, shown in *Figure 24,* displays a Bragg diffraction peak at $2\theta = 28.82°$ due to the C (002) crystal plane index. This corresponds to a d_{002} spacing of 0.31 nm, slightly smaller than the interlayer spacing of graphite (0.334 nm) [93]. The smaller interlayer spacing may result from the introduction of oxygen-containing groups between graphite layers during synthesis. Oxygen groups create active centres in the nanoparticles, which may help to increase packing by forming strong bonds between carbon and oxygen. Furthermore, lower d_{002} spacing is indicative of a low quantity of defects in the lattice structure, which further allows the layers to orient more tightly[109]. The interlayer spacing is considerably smaller than that of hydrothermally synthesised GQDs, indicative of a lower degree of basal plane functionalisation, the reasons for which will be explained later.

The second peak at $2\theta = 40.07°$ corresponds to the d_{100} plane index (length of the unit cell) and is equivalent to 0.22 nm, again slightly smaller than that of graphite (0.246 nm) [94]. Considering that

both lattice parameters are ~0.025 nm smaller than graphitic values, it is entirely possible that the values differ due to experimental error. The electrochemical synthesis resulted in a more dilute solution of GQDs than hydrothermal synthesis, so the distribution of EC1 nanoparticles on the glass substrate may not have been as even. Furthermore, fewer nanoparticles may have been present in the sample. Both factors could affect the diffraction peak values, and further experimentation is required for confirmation.
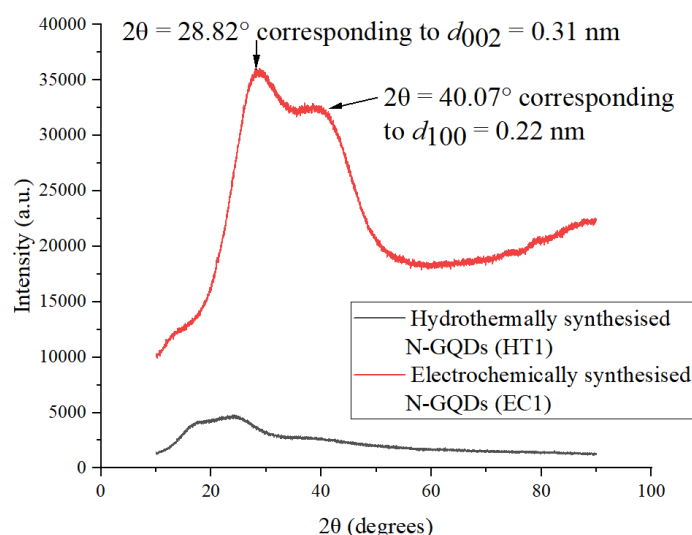
Figure 24: *XRD graph of electrochemically synthesised N-GQDs. Sample EC1 is shown in red and sample HT1 is shown in black and is included for comparison between intensity and peak positions.*

The higher peak intensity of EC1 compared to HT1 is indicative of a differing morphology between the nanoparticles[110], which will be discussed in detail in section 4.4.

Table 3: *Comparison of synthesised N-GQDs. Samples HT1 and EC1 were synthesised in this work and are described above, while the final sample data was obtained from literature for comparison of electrochemical synthesis.*

Sample name	Synthesis method/ time	Particle size/ nm	Bandgap/ eV
HT1	Hydrothermal (microwave) 150 s	5	2.50
EC1	Electrochemical cutting 1 hour	6	3.01
N-GQDs derived from carbon cloth [111]	Electrochemical cutting 24 hours	3.1	2.83

4.4. Edge Shapes

UV-Vis spectra of N-GQD samples synthesised through both synthetic methods were produced for samples with varied pHs (*Figure 25*). The pH of the N-GQD solutions were adjusted with nitric acid

and sodium bicarbonate. It was found that the N-GQDs produced through the hydrothermal microwave-assisted synthesis (HT1) exhibited changes in the wavelength absorption upon pH variation. In contrast, the N-GQDs produced electrochemically (EC1) displayed no changes in peak position.

Reports in the literature state that the bandgap of GQDs is pH dependent[75],[112]; however based on the obtained UV-Vis spectra (*Figure 25*), it has been found that this is not true of all GQDs. An explanation for this results from considering the edge structure of ZZ and AC-edged GQDs.

ZZ GQDs contain a carbene-like double bond on their edges and therefore possess a dangling bond which can be readily protonated or deprotonated. When ZZ GQDs are exposed to a low pH, their edges will protonate, increasing the size of the sp^2 domain and thus narrowing their bandgap. The opposite will be true for ZZ GQDs suspended in basic media, whereby their edges will deprotonate, decreasing the sp^2 domain and hence widening their bandgap. The shifts in wavelength absorption upon changing pH of the ZZ GQDs (*Figure 25a*) are similar to previously reported shifts in UV-Vis spectra of GQDs when the solution pH has been altered, whereby redshift is seen upon decreasing pH[20]. This has been shown to correlate with bandgap size, with bandgap increasing as the solution becomes more basic[112].

AC edges will not be affected by the variations in the pH of their solvent. Armchair-edged GQDs have a carbyne-like triple bond and hence have no free bonds available to protonate/ deprotonate. This therefore suggests that hydrothermally synthesised GQDs contain ZZ edges, while electrochemically synthesised GQDs contain only AC edges. The differing morphology is supported by the variation in the intensity of diffraction peaks in the XRD graphs of the samples (*Figure 24*).

The implications of the bandgap changes upon pH variation are of extreme significance to any electrochemical device with zigzag GQDs integrated into their electrodes. The pH of the electrolyte used in the cell will impact the performance of these GQDs. If an electrolyte that excessively widens or narrows the bandgap is selected, it will hinder the performance of the device, whilst if an ideal electrolyte is selected, the performance will be enhanced.
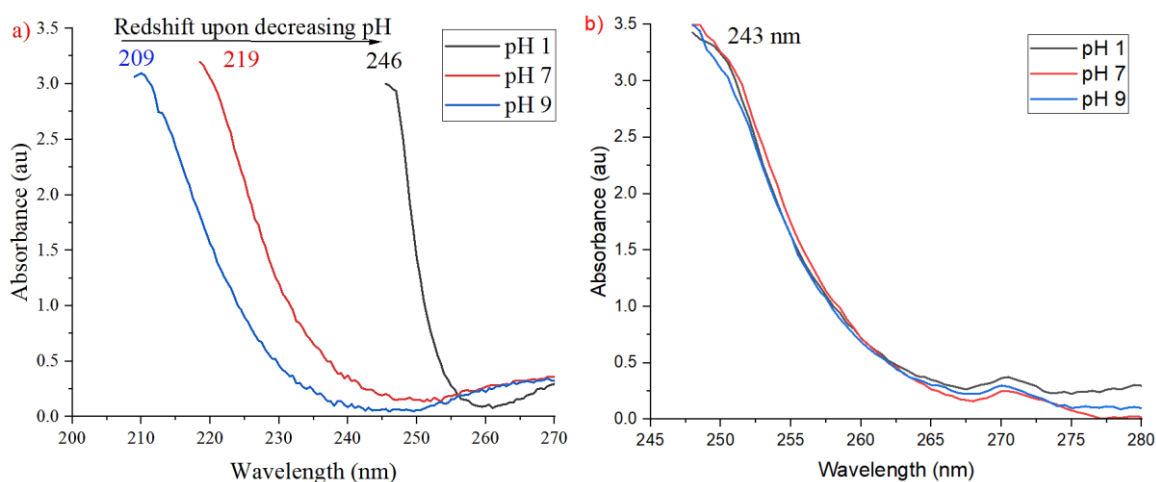
Figure 25: *UV-Vis spectra at varied pH levels of a) hydrothermally synthesised GQDs (ZZ GQDs; HT1) and b) electrochemically synthesised GQDs (AC GQDs; EC1)*

The wider bandgap of the AC GQDs compared to that for all sizes of ZZ GQDs is expected. The synthesised AC GQDs are of a similar size to HT1, the ZZ GQDs with the smallest lateral dimensions, and it is known that AC GQDs will always display a larger bandgap than ZZ GQDs of the same size. This is a direct consequence of the dispersionless edge states present in ZZ GQDs that are not observed in AC GQDs[21]. The degenerate zero energy edge states in the ZZ GQDs follow Hund's rule and allow additional energy level transitions that do not occur in AC GQDs. The bandgap difference between ZZ and AC GQDs is more evident for smaller GQDs as the ratio of edge atoms to central atoms is increased. Moreover, it has been demonstrated that the functionalisation of GQDs narrows the bandgap of ZZ GQDs more than AC GQDs, and so the significant difference between the bandgaps of HT1 and EC1 can be further attributed to the larger quantity of functional groups on HT1[113].

The specific capacitance of the CFs with ZZ GQDs deposited was 60 F/g, compared to 31 F/g for CFs with AC GQDs in 1 M H_2SO_4 electrolyte. The dangling bonds present at the edges of ZZ GQDs increase their affinity for edge site doping, allowing Faradaic groups to attach and thus improving their pseudocapacitive storage capability. The cyclic voltammograms are shown for carbon fibre electrodes with HT1 and EC1 deposited on their surfaces (*Figure 26*), demonstrating the increased quantity of redox reactions for HT1 compared to EC1.

Furthermore, the ZZ GQDs possess a higher degree of functionalisation than AC GQDs, as can be seen from the increased interlayer spacing given by XRD analysis when compared to AC GQDs (*Figure 24*). The spacing suggests that AC GQDs have very limited, if any, basal plane functionalisation between layers by oxygen and amine groups. Synthesising GQDs from a bottom-up technique (ZZ GQDs) is more likely to result in defects to the lattice structure since smaller organic

molecules must pyrolyse and stack to form the GQDs under high temperatures. Contrary to this, the top-down synthetic technique from graphite rods (AC GQDs) only requires that electrochemical exfoliation of high-purity graphite occurs. The layers will break apart where OH⁻ ions have intercalated into the graphite rod, meaning the resulting nanoparticle will be unlikely to have any hydroxyl groups between the layers of the synthesised GQD, since if penetration of OH⁻ ions had occurred between the layers, the particle would have been electrochemically cut at this position under the influence of the applied potential. Any functionalisation with oxygen-containing or amine groups is thus limited to the external basal plane (i.e. on the top and bottom of the GQD) and edges of the nanoparticle. The wider interlayer spacing and increased functionalisation of the ZZ GQDs results in increased wettability, alongside higher redox energy storage capabilities due to the larger number of sites available for Faradaic reactions to occur compared to AC GQDs.

The redox capabilities demonstrated by the AC GQDs, albeit somewhat limited, originate from the functionalisation of their edges with oxygen and amine groups, alongside nitrogen doping. Defects were induced by heating the graphite rods during synthesis, which allowed nitrogen doping to occur at these defect sites. Moreover, the electrochemical cleaving of carbon bonds during synthesis created further sites for doping. This introduced Faradaic groups to the nanoparticles, allowing some pseudocapacitive charge storage to occur.
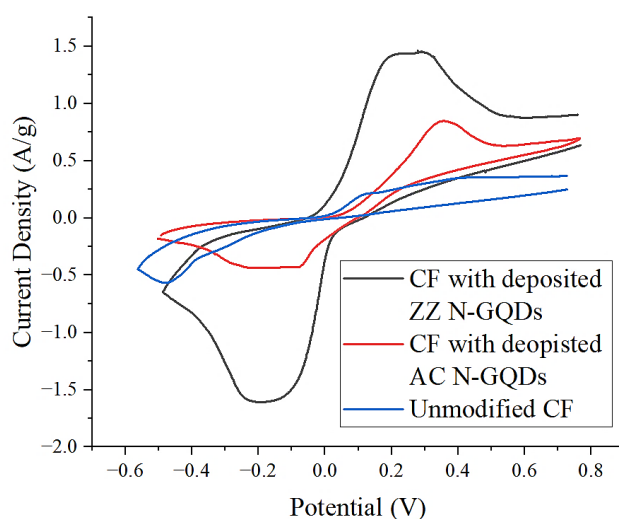
Figure 26: *Cyclic voltammograms at 5 mV/s of carbon fibres with electrodeposited ZZ (black) and AC (red) N-GQDs and unmodified carbon fibres (blue) in 1M H_2SO_4 electrolyte.*

The specific capacitance of carbon fibres with AC GQDs deposited (31 F/g) is lower than that of pretreated-only CFs (37 F/g). This is explained by the Faradaic processes on the electrodes. The oxygen-containing functional groups that are introduced to carbon fibres through pre-treatment are able to participate in redox reactions. However, these active sites are effectively 'used up' during

GQD deposition (GQDs bond to the oxygen groups), and the deposited AC GQDs have fewer available redox sites than the oxygenated CFs, resulting in a lower specific capacitance.

Table 4: *Specific capacitances obtained from cyclic voltammetry for carbon fibre-based electrodes.*

Electrode	Specific Capacitance/ F/g
Unmodified carbon fibres	16
Pretreated only carbon fibres	37
Carbon fibres with HT1 (ZZ N-GQDs) deposited	60
Carbon fibres with EC1 (AC N-GQDs) deposited	31

Owing to the increased energy storage capability of ZZ GQDs in comparison to AC GQDs, it is important to understand how ZZ GQDs interact with other components in energy storage devices. As previously mentioned, the bandgap of ZZ GQDs is easily tunable and will be affected by the electrolyte in use. Despite this, the selection of specific edge types of GQDs and considerations of how they interact with electrolytes are often ignored during the development of energy storage devices. Therefore, It is necessary to consider these factors and understand the chemical kinetics of the system in which the GQDs are embedded to reach device optimisation.

4.5. Density of States and Chemical Kinetics Calculations

The density of states (DOS) profiles of GQD samples are of significant interest in determining which size/ shape of GQDs will provide the best electrochemical properties to the electrode surfaces. The DOS profiles of the GQDs at the Fermi level provide insight into the chemical kinetics of the systems and their interaction with electrolytes since interfacial electron transfer is dependent on the availability of donor and acceptor sites. Despite this, *little work has been done to experimentally determine the DOS profiles of GQD samples before device integration*.

From here on, the electrodes will be referred to as ZZCF (carbon fibres with ZZ GQDs electrodeposited) and ACCF (carbon fibres with AC GQDs electrodeposited). The double layer capacitances were calculated according to the method described in section 3.5.1. The C_{dl} for ZZCF and ACCF were found to be 0.65 F/g and 0.49 F/g respectively. The higher C_{dl} value for the ZZCF electrodes can be explained by considering that EDL capacitance is increased upon increasing material surface area.

While the ZZ GQDs and AC GQDs display similar lateral dimensions, that does not necessarily equate to having an identical surface area. As a result of the acidic electrolyte used, it is likely that the ZZ GQD edges protonated, while the AC GQDs did not (due to the lack of dangling bonds at their edges).

This leads to a (slight) increase in the lateral dimensions of the ZZ GQDs via edge site doping, thus increasing their surface area. A more impactful factor to the surface area of the nanoparticles is their thickness, which was not measured directly. Based on previous reports, the thickness of GQDs is typically between 1 nm and 5 nm, depending on how many graphene layers are present in the particle[76]. Based on the TEM images of the nanoparticles, it is fairly likely that the ZZ GQDs (*Figure 15*) are thicker than the AC GQDs (*Figure 23*). On TEM images, thicker particles appear darker since the electron beam interacts more strongly with them. The imaged AC GQDs were lighter in colour than the ZZ GQDs, which may be indicative of particle thickness differences, further suggesting that ZZ GQDs have a larger surface area. This may result from the synthetic processes used to create the GQDs. Since the AC GQDs were synthesised by electrochemical cutting of graphite through hydroxyl group intercalation, the particles were likely cleaved on a layer-by-layer basis, which may have resulted in some polydispersity, leading to some single-layer GQDs and some GQDs with only a few layers. However, The microwave-assisted hydrothermal synthesis of ZZ GQDs would not have been restricted to few layered quantum dots. The nucleation process may have combined multiple single or few-layered graphene nanoparticles to form a single GQD. Furthermore, as previously mentioned, rapid heating during synthesis led to increased functionalisation with nitrogen, carboxyl and hydroxyl groups, as can be seen from the increased interlayer spacing given by XRD analysis of HT1 compared to EC1 (*Figure 24*). Increased branching through functionalisation will result in a less spherical particle, increasing surface area in comparison to particles with less functionalisation. The defects induced by rapid heating would further increase the surface area.

The double layer capacitance values were subsequently used to calculate the quantum capacitance. C_{total} values were obtained from the EIS plots described in section 3.5.1., but were conducted at different potentials, as is explained below, and the C_q values were calculated from equation (6). Capacitance values are frequency dependent due to localised dielectric polarisation effects. The quantum capacitance was therefore calculated for 10 kHz – 100 Hz.

To avoid errors relating to depletion and accumulation layers between the electrodes and the electrolyte, Mott Schottky analysis was used to determine the flatband potential (V_{fb}) for the ZZCF and ACCF electrodes in the half-cell configuration. This was necessary to determine a potential at which to produce EIS plots for each electrode from which the values of C_q were determined to ensure that the charge carriers at the electrode-electrolyte interface were in similar states for both electrodes, and differences in quantum capacitance measurements weren't a result of surface states. The N-GQD-modified electrodes were determined to be n-type based on the positive linear slope displayed in the Mott-Schottky graphs. The Mott Schottky graph for the ACCF electrode is shown in *Figure 27*. Pristine GQDs have been found to be p-type semiconductors[114], however the

n-type nature of the N-GQDs can be attributed to the electron-donating effects of the doped nitrogen atoms. The flat band potentials were determined to be 0.21 and 0.29 V vs. Ag/ AgCl standard reference electrode for ACCF and ZZCF, respectively.
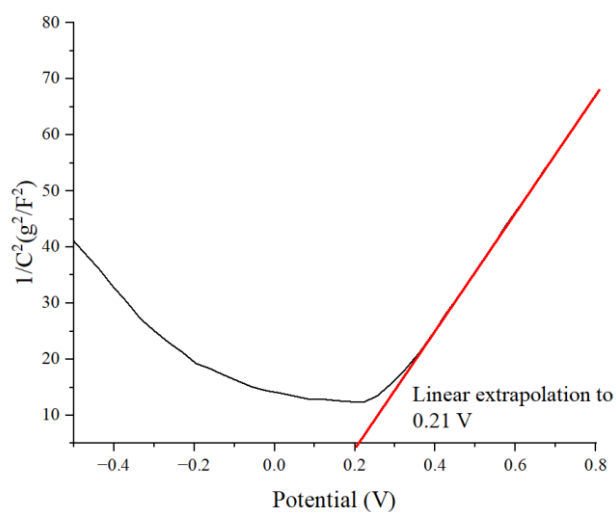
Figure 27: *Mott Schottky plot for AC GQDs (EC1) showing n-type conductivity with a flatband potential of 0.21V.*

EIS plots were obtained at the flat band potential for each electrode. At sufficiently low frequencies, the system can be modelled as a simple capacitor[115], whereby no kinetic limitations occur due to dissipative or propagative effects[116], and so the applied frequencies were kept relatively low (100 Hz – 10 kHz) (i.e. the impact of quantum capacitance is more prominent at low applied frequencies of the system [117] and therefore attention was paid to the low frequency capacitance values). The lowest frequency was selected to be 100 Hz as the GQDs displayed electric field reversal at lower frequencies, resulting from nonsynchronicity between the phases of the scan and internal accumulated carrier state in the GQDs[118]. *Figure 28* displays the quantum capacitance variation over the given range for both electrodes. It can be seen that C_q is larger for ZZCF for all frequencies. Quantum capacitance is directly proportional to the square root of the DOS, and the overall shape of the quantum capacitance profile is therefore the same as the shape of the DOS profile for the electrodes. A van-Hove singularity (peak) can be seen in the profile for ZZCF at ~8000 Hz and is indicative of the presence of edge states[119]. The singularity is likely only present for ZZCF since ZZ GQDs display dispersionless edge states, while AC GQDs do not.
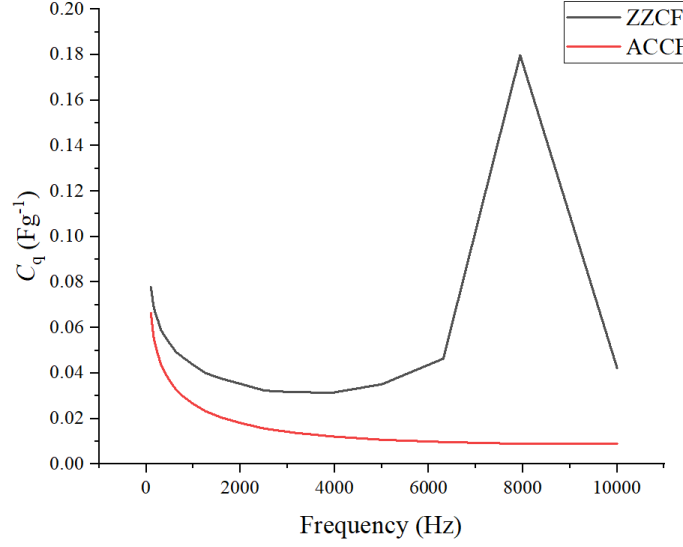
Figure 28: *Quantum capacitance profile for ZZCF and ACCF samples. The peak in the ZZCF profile is a van-Hove singularity, indicative of the presence of edge states.*

The dielectric permittivity of each sample is required before the DOS values can be obtained. It can be calculated from the surface area and thickness of the electrodes using equation (17).

$$\varepsilon = \frac{Cd}{A\varepsilon_0} \tag{17}$$

where C is the capacitance, d is the sample thickness, A is the surface area and ε_0 is vacuum permittivity[120].

The sample surface area can be found by the Brauner-Emmett-Teller (BET) method. In the BET method, the volume of gas adsorbed to the surface of the sample is measured as a function of the relative pressure. BET isotherms are then produced, from which the monolayer capacity of the adsorbed gas (n_m) can be obtained from the BET equation (18).

$$\frac{\frac{P}{P_0}}{n\left(1 - \frac{P}{P_0}\right)} = \frac{1}{n_m B} + \frac{B - 1}{n_m B}\left(\frac{P}{P_0}\right) \tag{18}$$

where P is the pressure, P_0 is the saturation pressure of the adsorbed gas at the set experiment temperature, n is the specific amount of adsorbed gas at the relative pressure, and B is a constant.

Volume-specific surface area (a_s) is subsequently determined from:

$$a_s = \frac{n_m L \sigma_m}{m} \tag{19}$$

with L, σ_m and m Avogadro's constant, the molecular cross-sectional area, and the mass of adsorbate, respectively [121].

Due to an inability to access a BET machine, the surface area measurements have yet to be carried out, however the remainder of the procedure to calculate the dielectric permittivity of the GQDs will be described. The surface area of the deposited GQDs is calculated by subtracting the surface area of the bare carbon fibres. Atomic force microscopy (AFM) can be used to measure the thickness of the deposited GQD layers, however care should be taken since the deposited layers on the surface of the carbon fibres are inhomogenous (a homogenous layer would result in aggregation of GQDs into graphene), and so some level of approximation and fitting of parameters may be necessary, i.e. it will likely be required to obtain an average and assume a uniform thickness of GQDs across the whole electrode surface.

Biswal *et al.*[122] directly measured the dielectric permittivity of GQDs using an Alpha-A high performance frequency analyser. Based on the physical characterisation of their synthesised GQDs, the obtained particles are comparable to sample HT1. Raman spectroscopy showed the presence of a G band at 1590 cm^{-1} and a D band at 1345 cm^{-1}, suggesting that the synthesised nanoparticles are zigzag-edged GQDs[123]. Furthermore, the obtained GQDs had a bandgap of 2.52 eV, close to the 2.5 eV bandgap of HT1. The dielectric permittivity was measured to be 2.5 x 10^4 at 100 Hz, and this is likely a ballpark figure for sample HT1. To note, the AC GQDs will have a different, presumably smaller, dielectric constant than the ZZ GQDs due to their differing capacitance, likely lower surface area, and possible differences in nanoparticle layer thickness on the electrode surface. The dielectric permittivity will only be this high for low-frequency values as an interfacial region can form at low frequencies, whereas at high frequencies relaxation processes do not occur as space charges do not have sufficient time to align. Furthermore, dipolar polarisation will only occur at low frequencies, whereby the permanent dipoles align under the applied electric field[122]. At frequencies of over ~10000 Hz, the dielectric permittivity becomes a relatively constant, low value. This is due to the light atoms which make up the GQDs and the weak spin-orbit coupling of the nanoparticles, leading to strong carrier-carrier interactions and well-defined spin multiplicity of electronic states[124].

DOS calculations can then be carried out for each of the samples using the obtained dielectric constant and equation (7), taking care to use the quantum capacitance value at the same frequency for which the dielectric permittivity was calculated. Once this DOS value has been determined, the rate constants for each GQD sample can be found using the calculated value:

$$k_f = k_t \cdot W_{red} \cdot DOS \tag{20}$$

$$k_b = k_t \cdot W_{ox} \cdot DOS \tag{21}$$

with k_f the oxidation rate constant, k_b the reduction rate constant and k_t the tunnelling probability constant. W_{red} and W_{ox} are probabilities of finding the empty/occupied state of the ions in the electrolytes and are calculated for the electrolyte in use:

$$W_{ox} = \frac{e}{\sqrt{4kT\lambda}} \, e^{\left(-\frac{(eV-eE_0+\lambda)^2}{4kT\lambda}\right)} \tag{22}$$

$$W_{red} = \frac{e}{\sqrt{4kT\lambda}} \, e^{\left(-\frac{(eV-eE_0-\lambda)^2}{4kT\lambda}\right)} \tag{23}$$

where E_o is the ion standard reduction potential (of the electrolyte), λ is the reorganisation energy associated with the redox process, k is the Boltzmann constant, T is the absolute temperature, e is elemental charge, and V is the voltage[125].

Using these calculations, the rate constants of GQD samples can be determined for any given electrolyte based on values of their ion reduction values, which can be experimentally measured or obtained from the literature. It should be noted that the double layer capacitance values will change depending on the concentration of the electrolyte in use[126], so to compare electrolytes of different concentrations the full procedure would have to be repeated for each electrolyte (but electrolytes of similar concentration are comparable without redetermining double layer capacitance). The electrochemical rate constants quantify the reversibility of the interfacial electron transfer reactions, providing an indication of the longevity of the electrode lifecycle. Furthermore, it has previously been discovered that increasing the rate constants at the active sites of the electrodes by one order of magnitude results in a 4% improvement in the specific energy and power of a lithium-ion battery[127], and will likely have similar effects on all electrochemical energy storage devices.

It is, however, worth emphasising that the synergistic effects of composite electrode materials will have a more significant impact than the lone GQDs deposited on electrode surfaces. This process of establishing reliable electrode kinetics is therefore not worth considering for the GQDs alone, but rather for the whole electrode. This method of establishing electrode kinetics is suitable. The

dielectric of the composite electrode can be found by determining the thickness and surface area of the electrode, and this can be used with the double layer capacitance for the composite electrode to determine its density of states. The addition of GQDs to electrodes has previously been shown to increase the dielectric constant of the material, alongside reducing dielectric loss[128].

Electrolytes for electrochemical energy storage devices are often selected on somewhat of a trial-and-error basis, a time, resource, and labour-intensive process[129]. Considerations are typically given to factors such as electrolyte conductivity, ion mobility, thermal stability, and dissociation ability. However, other characteristics, including achievable capacitance, voltage window, and cyclability are less reported [130]. Correct electrolyte selection is essential in the development of optimised energy storage devices; the electrolyte directly impacts charge storage mechanisms at the electrode-electrolyte interface. The process outlined above can be utilised to determine the suitability of electrolytes for energy storage devices, giving specific attention to factors that are not always considered. This will reduce trial-and-error-based testing, allowing easily obtained, experimentally determinable values to be used alongside data available in the literature to predict outcomes.

The knowledge of these values will allow for the effective selection of an electrolyte for a GQD-based energy storage device. This will allow for the optimisation of synergistic energy storage devices, whereby the GQD composite electrode materials and electrolytes can be successfully coordinated with each other's kinetic effects to create high-performance devices.

5. Conclusions

Nitrogen-doped GQDs were synthesised hydrothermally and electrochemically. The synthetical methods used were rapid, inexpensive, and scalable. UV-Vis spectra and electrochemical measurements suggest the hydrothermally synthesised N-GQDs possessed zigzag edges, while the electrochemically synthesised N-GQDs contained only armchair edges. The bandgap of ZZ-edged GQDs is affected by the pH of the electrolyte used in the energy storage device and must be considered in device fabrication, whereas this is not the case for armchair-edged GQDs.

Electrochemical measurements demonstrate that ZZ edged-GQDs display increased double layer capacitance due to their higher surface area, an increased pseudocapacitance attributed to their high affinity for edge-site doping with Faradaic groups, and a higher specific capacitance as a result of both these factors combined when compared to AC GQDs. It was also shown that ZZ-edged GQDs have a higher quantum capacitance, likely due to a higher density of states than AC GQDs, resulting from dispersionless edge states on ZZ GQDs. The combination of these factors provides evidence of the greater energy storage capability of ZZ-edged GQDs and verifies that they are the preferential GQD shape for boosting energy storage device performance.

A method of determining rate constants for individual GQD shapes and composite GQD electrodes has been highlighted. This can predict ideal electrolytes for electrochemical energy storage devices, reducing the need for trial-and-error-based testing. This critical information will be used to optimise the performance of energy storage devices utilising GQDs.

Further work should be carried out to ensure the smallest ZZ GQDs display preferential electrochemical properties when compared to larger nanoparticle sizes. Investigation into the exact degree of functionalisation and doping, alongside the exact nitrogen configurations, should also be conducted to analyse the impact of differences between nanoparticles.

References

[1]   R. Sharma, A., Gupta, M.K., Gupta, "Quantum Phenomena in Zero Dimensions :," *Int. J. Recent Innov. Trends Comput. Commun.*, vol. 1, no. April, pp. 18–22, 2016.

[2]   L. A. Ponomarenko *et al.*, "Chaotic dirac billiard in graphene quantum dots," *Science (80-.).*, vol. 320, no. 5874, pp. 356–358, 2008, doi: 10.1126/science.1154663.

[3]   M. H. M. Facure, R. Schneider, L. A. Mercante, and D. S. Correa, "A review on graphene quantum dots and their nanocomposites: From laboratory synthesis towards agricultural and environmental applications," *Environ. Sci. Nano*, vol. 7, no. 12, pp. 3710–3734, 2020, doi: 10.1039/d0en00787k.

[4]   Y. Yan *et al.*, "Recent Advances on Graphene Quantum Dots: From Chemistry and Physics to Applications," *Adv. Mater.*, vol. 31, no. 21, pp. 1–22, 2019, doi: 10.1002/adma.201808283.

[5]   M. Bacon, S. J. Bradley, and T. Nann, "Graphene quantum dots," *Part. Part. Syst. Charact.*, vol. 31, no. 4, pp. 415–428, 2014, doi: 10.1002/ppsc.201300252.

[6]   M. Hassan, E. Haque, K. R. Reddy, A. I. Minett, J. Chen, and V. G. Gomes, "Edge-enriched graphene quantum dots for enhanced photo-luminescence and supercapacitance," *Nanoscale*, vol. 6, no. 20, pp. 11988–11994, 2014, doi: 10.1039/c4nr02365j.

[7]   M. Kortel, B. D. Mansuriya, N. V. Santana, and Z. Altintas, "Graphene quantum dots as flourishing nanomaterials for bio-imaging, therapy development, and micro-supercapacitors," *Micromachines*, vol. 11, no. 9, 2020, doi: 10.3390/MI11090866.

[8]   I. Meric, M. Y. Han, A. F. Young, B. Ozyilmaz, P. Kim, and K. L. Shepard, "Current saturation in zero-bandgap, top-gated graphene field-effect transistors," *Nat. Nanotechnol.*, vol. 3, no. 11, pp. 654–659, 2008, doi: 10.1038/nnano.2008.268.

[9]   D. Torres, J. L. Pinilla, E. M. Gálvez, and I. Suelves, "Graphene quantum dots from fishbone carbon nanofibers," *RSC Adv.*, vol. 6, no. 54, pp. 48504–48514, 2016, doi: 10.1039/c6ra09679d.

[10]   A. B. Ghosh, N. Saha, A. Sarkar, D. N. Srivastava, P. Paul, and B. Adhikary, "Solvent assisted and solvent free orientation of growth of nanoscaled lanthanide sulfides: Tuning of morphology and manifestation of photocatalytic behavior," *RSC Adv.*, vol. 5, no. 124, pp. 102818–102827, 2015, doi: 10.1039/c5ra19959j.

[11]   K. S. Novoselov *et al.*, "Two-dimensional gas of massless Dirac fermions in graphene," *Nature*, vol. 438, no. 7065, pp. 197–200, 2005, doi: 10.1038/nature04233.

[12]   L. Ju *et al.*, "Tunable excitons in bilayer graphene," *Science*, vol. 358, no. 6365, pp. 907–910, 2017, doi: 10.1126/science.aam9175.

[13]   Y. Gu, Z. Qiu, and K. Müllen, "Nanographenes and Graphene Nanoribbons as Multitalents of Present and Future Materials Science," *J. Am. Chem. Soc.*, vol. 144, no. 26, pp. 11499–11524, 2022, doi: 10.1021/jacs.2c02491.

[14]   Z. Huang *et al.*, "Quantum confinement in graphene quantum dots," *Phys. Status Solidi - Rapid Res. Lett.*, vol. 8, no. 5, pp. 436–440, 2014, doi: 10.1002/pssr.201409064.

[15]   L. J. Yin, K. K. Bai, W. X. Wang, S. Y. Li, Y. Zhang, and L. He, "Landau quantization of Dirac fermions in graphene and its multilayers," *Front. Phys.*, vol. 12, no. 4, 2017, doi: 10.1007/s11467-017-0655-0.

[16]   A. D. Güçlü, P. Potasz, and P. Hawrylak, "Excitonic absorption in gate-controlled graphene

quantum dots," *Phys. Rev. B - Condens. Matter Mater. Phys.*, vol. 82, no. 15, pp. 1–5, 2010, doi: 10.1103/PhysRevB.82.155445.

[17]   R. Zhang *et al.*, "Size and refinement edge-shape effects of graphene quantum dots on UV-visible absorption," *J. Alloys Compd.*, vol. 623, pp. 186–191, 2015, doi: 10.1016/j.jallcom.2014.10.105.

[18]   S. He, M. J. Turnbull, Y. Nie, X. Sun, and Z. Ding, "Band structures of blue luminescent nitrogen-doped graphene quantum dots by synchrotron-based XPS," *Surf. Sci.*, vol. 676, pp. 51–55, 2018, doi: 10.1016/j.susc.2018.01.013.

[19]   H. Mondal, T. Dey, and R. Basori, "Silicon Nanowire Arrays with Nitrogen-Doped Graphene Quantum Dots for Photodetectors," *ACS Appl. Nano Mater.*, vol. 4, no. 11, pp. 11938–11948, 2021, doi: 10.1021/acsanm.1c02505.

[20]   J. P. Naik, P. Sutradhar, and M. Saha, "Molecular scale rapid synthesis of graphene quantum dots (GQDs)," *J. Nanostructure Chem.*, vol. 7, no. 1, pp. 85–89, 2017, doi: 10.1007/s40097-017-0222-9.

[21]   S. A. Oliaei Motlagh and V. Apalkov, "Absorption properties of graphene quantum dots under ultrashort optical pulses," *Phys. Rev. B*, vol. 104, no. 4, 2021, doi: 10.1103/PhysRevB.104.045421.

[22]   W. Hu *et al.*, "Room-temperature magnetism and tunable energy gaps in edge-passivated zigzag graphene quantum dots," *npj 2D Mater. Appl.*, vol. 3, no. 1, 2019, doi: 10.1038/s41699-019-0098-2.

[23]   L. Brey and H. A. Fertig, "Edge states and the quantized Hall effect in graphene," *Phys. Rev. B - Condens. Matter Mater. Phys.*, vol. 73, no. 19, pp. 1–6, 2006, doi: 10.1103/PhysRevB.73.195408.

[24]   Z. Z. Zhang, K. Chang, and F. M. Peeters, "Tuning of energy levels and optical properties of graphene quantum dots," *Phys. Rev. B - Condens. Matter Mater. Phys.*, vol. 77, no. 23, pp. 1–5, 2008, doi: 10.1103/PhysRevB.77.235411.

[25]   B. Bera, A. Chakraborty, T. Kar, P. Leuaa, and M. Neergat, "Density of States, Carrier Concentration, and Flat Band Potential Derived from Electrochemical Impedance Measurements of N-Doped Carbon and Their Influence on Electrocatalysis of Oxygen Reduction Reaction," *J. Phys. Chem. C*, vol. 121, no. 38, pp. 20850–20856, 2017, doi: 10.1021/acs.jpcc.7b06735.

[26]   R. Parsons, "Electrical Double Layer: Recent Experimental and Theoretical Developments," *Chem. Rev.*, vol. 90, no. 5, pp. 813–826, 1990, doi: 10.1021/cr00103a008.

[27]   M. Nakamura, N. Sato, N. Hoshi, and O. Sakata, "Outer helmholtz plane of the electrical double layer formed at the solid electrode-liquid interface," *ChemPhysChem*, vol. 12, no. 8, pp. 1430–1434, 2011, doi: 10.1002/cphc.201100011.

[28]   J. Sung and C. Shin, "Recent studies on supercapacitors with next-generation structures," *Micromachines*, vol. 11, no. 12, pp. 1–25, 2020, doi: 10.3390/mi11121125.

[29]   R. De Levie, "The structure of charged interfaces," *Sensors and Actuators*, vol. 1, pp. 97–109, 1981, doi: 10.1016/0250-6874(81)80007-8.

[30]   R. Burt, G. Birkett, and X. S. Zhao, "A review of molecular modelling of electric double layer capacitors," *Phys. Chem. Chem. Phys.*, vol. 16, no. 14, pp. 6519–6538, 2014, doi: 10.1039/c3cp55186e.

[31] N. S. Choi *et al.*, "Challenges facing lithium batteries and electrical double-layer capacitors," *Angew. Chemie - Int. Ed.*, vol. 51, no. 40, pp. 9994–10024, 2012, doi: 10.1002/anie.201201429.

[32] J. Libich, J. Máca, J. Vondrák, O. Čech, and M. Sedlaříková, "Supercapacitors: Properties and applications," *J. Energy Storage*, vol. 17, no. March, pp. 224–227, 2018, doi: 10.1016/j.est.2018.03.012.

[33] L. Zhang and X. S. Zhao, "Carbon-based materials as supercapacitor electrodes," *Chem. Soc. Rev.*, vol. 38, no. 9, pp. 2520–2531, 2009, doi: 10.1039/b813846j.

[34] Y. Hanlumyuang and P. Sharma, "Quantum capacitance: A perspective from physics to nanoelectronics," *Jom*, vol. 66, no. 4, pp. 660–663, 2014, doi: 10.1007/s11837-014-0934-y.

[35] T. Verkholyak, A. Kuzmak, A. A. Kornyshev, and S. Kondrat, "Less Is More: Can Low Quantum Capacitance Boost Capacitive Energy Storage?," *J. Phys. Chem. Lett.*, vol. 13, no. 47, pp. 10976–10980, 2022, doi: 10.1021/acs.jpclett.2c02968.

[36] Q. Xu, G. Yang, X. Fan, and W. Zheng, "Improving the quantum capacitance of graphene-based supercapacitors by the doping and co-doping: first-principles calculations," *ACS Omega*, vol. 4, no. 8, pp. 13209–13217, 2019, doi: 10.1021/acsomega.9b01359.

[37] R. Narayanan, H. Yamada, M. Karakaya, R. Podila, A. M. Rao, and P. R. Bandaru, "Modulation of the electrostatic and quantum capacitances of few layered graphenes through plasma processing," *Nano Lett.*, vol. 15, no. 5, pp. 3067–3072, 2015, doi: 10.1021/acs.nanolett.5b00055.

[38] G. Tan *et al.*, "Freestanding highly defect nitrogen-enriched carbon nanofibers for lithium ion battery thin-film anodes," *J. Mater. Chem. A*, vol. 5, no. 11, pp. 5532–5540, 2017, doi: 10.1039/c7ta00969k.

[39] J. Zhu *et al.*, "Defect-Engineered Graphene for High-Energy- and High-Power-Density Supercapacitor Devices," *Adv. Mater.*, vol. 28, no. 33, pp. 7185–7192, 2016, doi: 10.1002/adma.201602028.

[40] L. Sun *et al.*, "Nitrogen-doped graphene with high nitrogen level via a one-step hydrothermal reaction of graphene oxide with urea for superior capacitive energy storage," *RSC Adv.*, vol. 2, no. 10, pp. 4498–4506, 2012, doi: 10.1039/c2ra01367c.

[41] H. Wang *et al.*, "Nitrogen, Sulfur, Phosphorous Co-doped Interconnected Porous Carbon Nanosheets with High Defect Density for Enhancing Supercapacitor and Lithium-Ion Battery Properties," *ChemElectroChem*, vol. 5, no. 17, pp. 2367–2375, 2018, doi: 10.1002/celc.201800444.

[42] X. Feng *et al.*, "Untangling the respective effects of heteroatom-doped carbon materials in batteries, supercapacitors and the ORR to design high performance materials," *Energy Environ. Sci.*, vol. 14, no. 4, pp. 2036–2089, 2021, doi: 10.1039/d1ee00166c.

[43] H. Chen *et al.*, "Boron and nitrogen co-doped porous carbon with a high concentration of boron and its superior capacitive behavior," *Carbon N. Y.*, vol. 113, pp. 266–273, 2017, doi: 10.1016/j.carbon.2016.11.035.

[44] Z. Zeng, S. Chen, T. T. Y. Tan, and F. X. Xiao, "Graphene quantum dots (GQDs) and its derivatives for multifarious photocatalysis and photoelectrocatalysis," *Catal. Today*, vol. 315, no. September 2017, pp. 171–183, 2018, doi: 10.1016/j.cattod.2018.01.005.

[45] X. T. Zheng, A. Ananthanarayanan, K. Q. Luo, and P. Chen, "Glowing graphene quantum dots

and carbon dots: Properties, syntheses, and biological applications," *Small*, vol. 11, no. 14, pp. 1620–1636, 2015, doi: 10.1002/smll.201402648.

[46]   M. Zhang, W. Liu, R. Liang, R. Tjandra, and A. Yu, "Graphene quantum dot induced tunable growth of nanostructured MnCo2O4.5 composites for high-performance supercapacitors," *Sustain. Energy Fuels*, vol. 3, no. 9, pp. 2499–2508, 2019, doi: 10.1039/c9se00341j.

[47]   Y. J. Oh *et al.*, "Oxygen functional groups and electrochemical capacitive behavior of incompletely reduced graphene oxides as a thin-film electrode of supercapacitor," *Electrochim. Acta*, vol. 116, pp. 118–128, 2014, doi: 10.1016/j.electacta.2013.11.040.

[48]   P. Wagner *et al.*, "Band Gap Engineering via Edge-Functionalization of Graphene Nanoribbons," *J. Phys. Chem. C,* vol. 115, no. 50, pp. 26790-26796, 2013, doi: 10.1021/jp408695c.

[49]   H. Abdelsalam, H. Elhaes, M. A. Ibrahim, and A. Shams, "Tuning electronic propertiesin graphene quantum dots by chemical functionalization: Density functional theory calculations," *Chem. Phys. Lett.,* vol. 695, pp. 1–18, doi: 10.1016/j.cplett.2018.02.015.

[50]   A. Sheely, B. Gifford, S. Tretiak, and A. Bishop, "Tunable Optical Features of Graphene Quantum Dots from Edge Functionalization," *J. Phys. Chem. C*, vol. 125, no. 17, pp. 9244–9252, 2021, doi: 10.1021/acs.jpcc.1c00537.

[51]   S. Moghimian and P. Sangpour, "One-step hydrothermal synthesis of GQDs-MoS2 nanocomposite with enhanced supercapacitive performance," *J. Appl. Electrochem.*, vol. 50, no. 1, pp. 71–79, 2020, doi: 10.1007/s10800-019-01366-3.

[52]   O. Sangabathula and C. S. Sharma, "One-pot hydrothermal synthesis of molybdenum nickel sulfide with graphene quantum dots as a novel conductive additive for enhanced supercapacitive performance," *Mater. Adv.*, vol. 1, no. 8, pp. 2763–2772, 2020, doi: 10.1039/d0ma00593b.

[53]   S. Fleischmann *et al.*, "Pseudocapacitance: From Fundamental Understanding to High Power Energy Storage Materials," *Chem. Rev.*, vol. 120, no. 14, pp. 6738–6782, 2020, doi: 10.1021/acs.chemrev.0c00170.

[54]   J. Liu *et al.*, "Advanced Energy Storage Devices: Basic Principles, Analytical Methods, and Rational Materials Design," *Adv. Sci.*, vol. 5, no. 1, 2018, doi: 10.1002/advs.201700322.

[55]   N. R. Chodankar *et al.*, "True Meaning of Pseudocapacitors and Their Performance Metrics: Asymmetric versus Hybrid Supercapacitors," *Small*, vol. 16, no. 37, pp. 1–35, 2020, doi: 10.1002/smll.202002806.

[56]   P. Sharma and V. Kumar, "Current Technology of Supercapacitors: A Review," *J. Electron. Mater.*, vol. 49, no. 6, pp. 3520–3532, 2020, doi: 10.1007/s11664-020-07992-4.

[57]   K. Lee, H. Lee, Y. Shin, Y. Yoon, D. Kim, and H. Lee, "Highly transparent and flexible supercapacitors using graphene-graphene quantum dots chelate," *Nano Energy*, vol. 26, pp. 746–754, 2016, doi: 10.1016/j.nanoen.2016.06.030.

[58]   J. Xiao, R. Momen, and C. Liu, "Application of carbon quantum dots in supercapacitors: A mini review," *Electrochem. commun.*, vol. 132, p. 107143, 2021, doi: 10.1016/j.elecom.2021.107143.

[59]   S. Zhang, L. Sui, H. Dong, W. He, L. Dong, and L. Yu, "High-Performance Supercapacitor of Graphene Quantum Dots with Uniform Sizes," *ACS Appl. Mater. Interfaces*, vol. 10, no. 15, pp. 12983–12991, 2018, doi: 10.1021/acsami.8b00323.

[60] A. B. Ganganboina, A. D. Chowdhury, and R. Doong, "New Avenue for Appendage of Graphene Quantum Dots on Halloysite Nanotubes as Anode Materials for High Performance Supercapacitors," *ACS Sustainable Chem. Eng.*, vol. 5, no. 5, pp. 4930-4940, 2017, doi: 10.1021/acssuschemeng.7b00329.

[61] H. Jia *et al.*, "Heterostructural Graphene Quantum Dot/MnO2 Nanosheets toward High-Potential Window Electrodes for High-Performance Supercapacitors," *Adv. Sci.*, vol. 5, no. 5, pp. 1–10, 2018, doi: 10.1002/advs.201700887.

[62] Y. Hong, J. Xu, J. S. Chung, and W. M. Choi, "Graphene quantum dots/Ni(OH)2 nanocomposites on carbon cloth as a binder-free electrode for supercapacitors," *J. Mater. Sci. Technol.*, vol. 58, pp. 73–79, 2020, doi: 10.1016/j.jmst.2020.03.063.

[63] Y. Qing *et al.*, "Boosting the supercapacitor performance of activated carbon by constructing overall conductive networks using graphene quantum dots," *J. Mater. Chem. A*, vol. 7, no. 11, pp. 6021–6027, 2019, doi: 10.1039/c8ta11620b.

[64] P. R. Kharangarh, V. Gupta, A. Singh, P. Bhardwaj, and A. N. Grace, "An efficient pseudocapacitor electrode material with co-doping of iron (II) and sulfur in luminescent graphene quantum dots," *Diam. Relat. Mater.*, vol. 107, p. 107913, 2020, doi: 10.1016/j.diamond.2020.107913.

[65] H. Kuzhandaivel, S. Manickam, S. K. Balasingam, M. C. Franklin, H. J. Kim, and K. S. Nallathambi, "Sulfur and nitrogen-doped graphene quantum dots/PANI nanocomposites for supercapacitors," *New J. Chem.*, vol. 45, no. 8, pp. 4101–4110, 2021, doi: 10.1039/d1nj00038a.

[66] L. Zhang and C. Chen, "Electrode materials for lithium ion battery," *Prog. Chem.*, vol. 23, no. 2–3, pp. 275–283, 2011, doi: 10.1007/978-0-85729-745-7_1.

[67] S. Huang, X. Zhu, S. Sarkar, and Y. Zhao, "Challenges and opportunities for supercapacitors," *APL Mater.*, vol. 7, no. 10, 2019, doi: 10.1063/1.5116146.

[68] J. Vetter *et al.*, "Ageing mechanisms in lithium-ion batteries," *J. Power Sources*, vol. 147, no. 1–2, pp. 269–281, 2005, doi: 10.1016/j.jpowsour.2005.01.006.

[69] W. Zhang, T. Xu, Z. Liu, N. L. Wu, and M. Wei, "Hierarchical TiO2-: X imbedded with graphene quantum dots for high-performance lithium storage," *Chem. Commun.*, vol. 54, no. 12, pp. 1413–1416, 2018, doi: 10.1039/c7cc09406j.

[70] J. Shim *et al.*, "Conductive Co3O4/graphene (core/shell) quantum dots as electrode materials for electrochemical pseudocapacitor applications," *Compos. Part B Eng.*, vol. 130, pp. 230–235, 2017, doi: 10.1016/j.compositesb.2017.07.039.

[71] Y. Wu and C. Cao, "The way to improve the energy density of supercapacitors: Progress and perspective," *Sci. China Mater.*, vol. 61, no. 12, pp. 1517–1526, 2018, doi: 10.1007/s40843-018-9290-y.

[72] M. Huda, "Epitaxial growth of lateral graphene / hexagonal boron nitride heterostructures", 2016.

[73] D. Chao *et al.*, "Graphene quantum dots coated VO2 arrays for highly durable electrodes for Li and Na ion batteries," *Nano Lett.*, vol. 15, no. 1, pp. 565–573, 2015, doi: 10.1021/nl504038s.

[74] J. Guo, H. Zhu, Y. Sun, L. Tang, and X. Zhang, "Boosting the lithium storage performance of MoS2 with graphene quantum dots," *J. Mater. Chem. A*, vol. 4, no. 13, pp. 4783–4789, 2016,

doi: 10.1039/c6ta00592f.

[75]   M. Aghelifar and S. Kimiagar, "pH effect on the size of graphene quantum dot synthesized by using pulse laser irradiation," *Phys. Chem. Res.*, vol. 6, no. 2, pp. 237–250, 2018, doi: 10.22036/pcr.2017.98758.1417.

[76]   Q. Ren, L. Ga, and J. Ai, "Rapid Synthesis of Highly Fluorescent Nitrogen-Doped Graphene Quantum Dots for Effective Detection of Ferric Ions and as Fluorescent Ink," *ACS Omega*, vol. 4, no. 14, pp. 15842–15848, 2019, doi: 10.1021/acsomega.9b01612.

[77]   S. Ahirwar, S. Mallick, and D. Bahadur, "Electrochemical Method to Prepare Graphene Quantum Dots and Graphene Oxide Quantum Dots," *ACS Omega*, vol. 2, no. 11, pp. 8343–8353, 2017, doi: 10.1021/acsomega.7b01539.

[78]   R. Tjandra, W. Liu, M. Zhang, and A. Yu, "All-carbon flexible supercapacitors based on electrophoretic deposition of graphene quantum dots on carbon cloth," *J. Power Sources*, vol. 438, no. July, p. 227009, 2019, doi: 10.1016/j.jpowsour.2019.227009.

[79]   N. Elgrishi, K. J. Rountree, B. D. McCarthy, E. S. Rountree, T. T. Eisenhart, and J. L. Dempsey, "A Practical Beginner's Guide to Cyclic Voltammetry," *J. Chem. Educ.*, vol. 95, no. 2, pp. 197–206, 2018, doi: 10.1021/acs.jchemed.7b00361.

[80]   S. Palchoudhury, K. Ramasamy, R. K. Gupta, and A. Gupta, "Flexible supercapacitors: A materials perspective," *Front. Mater.*, vol. 5, pp. 1–9, 2019, doi: 10.3389/fmats.2018.00083.

[81]   D. M. Morales and M. Risch, "Seven steps to reliable cyclic voltammetry measurements for the determination of double layer capacitance," *JPhys Energy*, vol. 3, no. 3, 2021, doi: 10.1088/2515-7655/abee33.

[82]   P. Makuła, M. Pacia, and W. Macyk, "How To Correctly Determine the Band Gap Energy of Modified Semiconductor Photocatalysts Based on UV-Vis Spectra," *J. Phys. Chem. Lett.*, vol. 9, no. 23, pp. 6814–6817, 2018, doi: 10.1021/acs.jpclett.8b02892.

[83]   M. Mamouei, K. Budidha, N. Baishya, M. Qassem, and P. A. Kyriacou, "An empirical investigation of deviations from the Beer–Lambert law in optical estimation of lactate," *Sci. Rep.*, vol. 11, no. 1, pp. 1–9, 2021, doi: 10.1038/s41598-021-92850-4.

[84]   W. Q. Hong, "Extraction of extinction coefficient of weak absorbing thin films from special absorption," *J. Phys. D. Appl. Phys.*, vol. 22, no. 9, pp. 1384–1385, 1989, doi: 10.1088/0022-3727/22/9/024.

[85]   M. Wiśniewski, "The Consequences of Water Interactions with Nitrogen-Containing Carbonaceous Quantum Dots—The Mechanistic Studies," *Int. J. Mol. Sci.*, vol. 23, no. 22, 2022, doi: 10.3390/ijms232214292.

[86]   F. K. -Moravvej, "Electronic Properties of Various Graphene Quantum Dot Structures: an Ab Initio Study," *Tabriz J. Electr. Eng.*, vol. 51, no. 2, 2021.

[87]   M. Kaur, M. Kaur, and V. K. Sharma, "Nitrogen-doped graphene and graphene quantum dots: A review onsynthesis and applications in energy, sensors and environment," *Adv. Colloid Interface Sci.*, vol. 259, pp. 44–64, 2018, doi: 10.1016/j.cis.2018.07.001.

[88]   M. T. Dejpasand, S. Sharifi, E. Saievar-Iranizad, A. Yazdani, and K. Rahimi, "Boron- and nitrogen-doped graphene quantum dots with enhanced supercapacitance," *J. Energy Storage*, vol. 42, no. May, p. 103103, 2021, doi: 10.1016/j.est.2021.103103.

[89]   P. Cui and Y. Xue, "The role of center-N-doping in non-radiative recombination loss of nitrogen-doped graphene quantum dots," *Mater. Sci. Semicond. Process.*, vol. 139, no.

September 2021, p. 106323, 2022, doi: 10.1016/j.mssp.2021.106323.

[90]   H. J. Lee *et al.*, "Understanding the impact of nitrogen doping and/or amine functionalization of reduced graphene oxide via hydrothermal routes for supercapacitor applications," *Electrochim. Acta*, vol. 397, p. 139241, 2021, doi: 10.1016/j.electacta.2021.139241.

[91]   Q. Xu *et al.*, "Recent progress of quantum dots for energy storage applications," *Carbon Neutrality*, vol. 1, no. 1, pp. 1–18, 2022, doi: 10.1007/s43979-022-00002-y.

[92]   X. Wang, H. Tang, S. Huang, and L. Zhu, "Fast and facile microwave-assisted synthesis of graphene oxide nanosheets," *RSC Adv.*, vol. 4, no. 104, pp. 60102–60105, 2014, doi: 10.1039/c4ra12022a.

[93]   B. Zheng *et al.*, "Ultrafast ammonia-driven, microwave-assisted synthesis of nitrogen-doped graphene quantum dots and their optical properties," *Nanophotonics*, vol. 6, no. 1, pp. 259–267, 2017, doi: 10.1515/nanoph-2016-0102.

[94]   D. M. Stefanescu, G. Alonso, P. Larrañaga, E. De La Fuente, and R. Suarez, "On the crystallization of graphite from liquid iron-carbon-silicon melts," *Acta Mater.*, vol. 107, pp. 102–126, 2016, doi: 10.1016/j.actamat.2016.01.047.

[95]   D. Tahir and K. H. Jae, "Effect of growth temperature on structural and electronic properties of ZnO thin films," *AIP Conf. Proc.*, vol. 1801, 2017, doi: 10.1063/1.4973085.

[96]   L. Tang *et al.*, "Deep ultraviolet photoluminescence of water-soluble self-passivated graphene quantum dots," *ACS Nano*, vol. 6, no. 6, pp. 5102–5110, 2012, doi: 10.1021/nn300760g.

[97]   P. Rani, R. Dalal, S. Srivastava, and K. Tankeshwar, "Tuning the properties of graphene quantum dots by passivation," *Phys. Chem. Chem. Phys.*, vol. 18, pp. 26232–26240, 2022, doi: 10.1039/d2cp03990g.

[98]   S. T. Harry and M. . Adekanmbi, "Confinement Energy of Quantum Dots and the Brus Equation," *Int. J. Res.*, vol. 8, no. 11, pp. 318–323, 2020, doi: 10.29121/granthaalayah.v8.i11.2020.2451.

[99]   K. A. Ritter and J. W. Lyding, "The influence of edge structure on the electronic properties of graphene quantum dots and nanoribbons," *Nat. Mater.*, vol. 8, no. 3, pp. 235–242, 2009, doi: 10.1038/nmat2378.

[100]   Y. Yan *et al.*, "Systematic Bandgap Engineering of Graphene Quantum Dots and Applications for Photocatalytic Water Splitting and CO2 Reduction," *ACS Nano*, vol. 12, no. 4, pp. 3523–3532, 2018, doi: 10.1021/acsnano.8b00498.

[101]   A. P. de M. Rocha, M. I. Alayo, and D. M. da Silva, "Synthesis of Nitrogen-Doped Graphene Quantum Dots from Sucrose Carbonization," *Appl. Sci.*, vol. 12, no. 17, 2022, doi: 10.3390/app12178686.

[102]   W. I. W. Omar, C. F. Soon, M. K. Ahmad, and M. Shimomura, "Hydrothermal synthesis of biocompatible nitrogen doped graphene quantum dots," *Energy Environ.*, vol. 32, no. 7, pp. 1170–1182, 2021, doi: 10.1177/0958305X20984112.

[103]   S. Kundu and V. K. Pillai, "Synthesis and characterization of graphene quantum dots," *Phys. Sci. Rev.*, vol. 5, no. 4, pp. 1–35, 2020, doi: 10.1515/psr-2019-0013.

[104]   Y. Liu, R. Wang, J. Lang, and X. Yan, "Insight into the formation mechanism of graphene quantum dots and the size effect on their electrochemical behaviors," *Phys. Chem. Chem. Phys.*, vol. 17, no. 21, pp. 14028–14035, 2015, doi: 10.1039/c5cp00646e.

[105] H. Wang *et al.*, "Ultramicroporous carbon cloth for flexible energy storage with high areal capacitance," *Energy Storage Mater.*, vol. 7, no. February, pp. 216–221, 2017, doi: 10.1016/j.ensm.2017.03.002.

[106] Q. Chen *et al.*, "Graphene quantum dots-three-dimensional graphene composites for high-performance supercapacitors," *Phys. Chem. Chem. Phys.*, vol. 16, no. 36, pp. 19307–19313, 2014, doi: 10.1039/c4cp02761b.

[107] E. Tegou, G. Pseiropoulos, M. K. Filippidou, and S. Chatzandroulis, "Low-temperature thermal reduction of graphene oxide films in ambient atmosphere: Infra-red spectroscopic studies and gas sensing applications," *Microelectron. Eng.*, vol. 159, pp. 146–150, 2016, doi: 10.1016/j.mee.2016.03.030.

[108] S. T. Hossain and R. Wang, "Electrochemical Exfoliation of Graphite: Effect of Temperature and Hydrogen Peroxide Addition," *Electrochim. Acta*, vol. 216, pp. 253–260, 2016, doi: 10.1016/j.electacta.2016.09.022.

[109] D. A. L. Almeida, A. B. Couto, S. S. Oishi, and N. G. Ferreira, "Chemical and electrochemical treatment effects on the morphology, structure, and electrochemical performance of carbon fiber with different graphitization indexes," *J. Solid State Electrochem.*, vol. 22, no. 11, pp. 3493–3505, 2018, doi: 10.1007/s10008-018-4037-5.

[110] M. Inoue and I. Hirasawa, "The relationship between crystal morphology and XRD peak intensity on CaSO4·2H2O," *J. Cryst. Growth*, vol. 380, pp. 169–175, 2013, doi: 10.1016/j.jcrysgro.2013.06.017.

[111] F. Yang *et al.*, "Nitrogen-doped graphene quantum dots prepared by electrolysis of nitrogen-doped nanomesh graphene for the fluorometric determination of ferric ions," *Microchim. Acta*, vol. 187, no. 6, 2020, doi: 10.1007/s00604-020-04294-8.

[112] C. Zhu *et al.*, "Negative induction effect of graphite N on graphene quantum dots: Tunable band gap photoluminescence," *J. Mater. Chem. C*, vol. 3, no. 34, pp. 8810–8816, 2015, doi: 10.1039/c5tc01933h.

[113] T. Basak and T. Basak, "Edge Modification and Site-Selective Functionalization of Graphene Quantum Dots: A Versatile Technique for Designing Tunable Optoelectronic and Sensing Devices," 2023, doi: 10.1021/acs.jpca.3c01600.

[114] K. A. Tsai *et al.*, "Nitrogen-Doped Graphene Quantum Dots for Remarkable Solar Hydrogen Production," *ACS Appl. Energy Mater.*, vol. 3, no. 6, pp. 5322–5332, 2020, doi: 10.1021/acsaem.0c00335.

[115] P. R. Bueno, F. C. Bedatty Fernandes, and J. J. Davis, "Quantum capacitance as a reagentless molecular sensing element," *Nanoscale*, vol. 9, no. 40, pp. 15362–15370, 2017, doi: 10.1039/c7nr06160a.

[116] M. C. Dartiailh *et al.*, "Dynamical Separation of Bulk and Edge Transport in HgTe-Based 2D Topological Insulators," *Phys. Rev. Lett.*, vol. 124, no. 7, p. 76802, 2020, doi: 10.1103/PhysRevLett.124.076802.

[117] P. R. Bueno and J. J. Davis, "Measuring quantum capacitance in energetically addressable molecular layers," *Anal. Chem.*, vol. 86, no. 3, pp. 1337–1341, 2014, doi: 10.1021/ac403135b.

[118] M. Guan, L. Niu, Y. Zhang, X. Liu, Y. Li, and Y. Zeng, "Space charges and negative capacitance effect in organic light-emitting diodes by transient current response analysis," *RSC Adv.*, vol. 7, no. 80, pp. 50598–50602, 2017, doi: 10.1039/c7ra07311a.

[119] S. Pratap, S. Kumar, and R. P. Singh, "Certain Aspects of Quantum Transport in Zigzag Graphene Nanoribbons," *Front. Phys.*, vol. 10, no. July, pp. 1–12, 2022, doi: 10.3389/fphy.2022.940586.

[120] K. Ulutas, D. Deger, and S. Yakut, "Thickness dependence of the dielectric properties of thermally evaporated Sb2Te3 thin films," *J. Phys. Conf. Ser.*, vol. 417, no. 1, pp. 0–6, 2013, doi: 10.1088/1742-6596/417/1/012040.

[121] F. Ambroz, T. J. Macdonald, V. Martis, and I. P. Parkin, "Evaluation of the BET theory for the characterization of meso and microporous MOFs," *Small Methods*, vol. 2, no. 11, pp. 1–17, 2018, doi: 10.1002/smtd.201800173.

[122] R. Biswal, B. Khan, and M. K. Singh, "Synthesis, optical, dielectric, and magneto-dielectric properties of graphene quantum dots (GQDs)," *J. Mater. Res.*, vol. 37, no. 20, pp. 3459–3469, 2022, doi: 10.1557/s43578-022-00717-9.

[123] J. Kim *et al.*, "Distinguishing Zigzag and Armchair Edges on Graphene Nanoribbons by X-ray Photoelectron and Raman Spectroscopies," *ACS Omega*, vol. 3, no. 12, pp. 17789–17796, 2018, doi: 10.1021/acsomega.8b02744.

[124] L. S. Li and X. Yan, "Colloidal graphene quantum dots," *J. Phys. Chem. Lett.*, vol. 1, no. 17, pp. 2572–2576, 2010, doi: 10.1021/jz100862f.

[125] M. R. Zoric *et al.*, "Electron Transfer Kinetics at Graphene Quantum Dot Assembly Electrodes," *ACS Appl. Mater. Interfaces*, vol. 11, no. 49, pp. 46303–46310, 2019, doi: 10.1021/acsami.9b14161.

[126] J. Xia, F. Chen, J. Li, and N. Tao, "Measurement of the quantum capacitance of graphene," *Nat. Nanotechnol.*, vol. 4, no. 8, pp. 505–509, 2009, doi: 10.1038/nnano.2009.177.

[127] V. Chabot, S. Farhad, Z. Chen, A. S. Fung, A. Yu, and F. Hamdullahpur, "Effect of electrode physical and chemical properties on lithium-ion battery performance," *Int. J. Energy Res.*, vol. 37, no. 14, pp. 1723–1736, 2013, doi: 10.1002/er.3114.

[128] T. Chen and B. Liu, "Dielectric properties of graphene quantum dot-cobalt ferrite-poly(vinylidene fluoride) ternary composites," *Mater. Lett.*, vol. 209, pp. 163–166, 2017, doi: 10.1016/j.matlet.2017.07.088.

[129] H. Liu, S. Ma, J. Wu, Y. Wang, and X. Wang, "Recent Advances in Screening Lithium Solid-State Electrolytes Through Machine Learning," *Front. Energy Res.*, vol. 9, pp. 1–8, 2021, doi: 10.3389/fenrg.2021.639741.

[130] B. Pal, S. Yang, S. Ramesh, V. Thangadurai, and R. Jose, "Electrolyte selection for supercapacitive devices: A critical review," *Nanoscale Adv.*, vol. 1, no. 10, pp. 3807–3835, 2019, doi: 10.1039/c9na00374f.